



저작자표시-비영리-변경금지 2.0 대한민국

이용자는 아래의 조건을 따르는 경우에 한하여 자유롭게

- 이 저작물을 복제, 배포, 전송, 전시, 공연 및 방송할 수 있습니다.

다음과 같은 조건을 따라야 합니다:



저작자표시. 귀하는 원저작자를 표시하여야 합니다.



비영리. 귀하는 이 저작물을 영리 목적으로 이용할 수 없습니다.



변경금지. 귀하는 이 저작물을 개작, 변형 또는 가공할 수 없습니다.

- 귀하는, 이 저작물의 재이용이나 배포의 경우, 이 저작물에 적용된 이용허락조건을 명확하게 나타내어야 합니다.
- 저작권자로부터 별도의 허가를 받으면 이러한 조건들은 적용되지 않습니다.

저작권법에 따른 이용자의 권리는 위의 내용에 의하여 영향을 받지 않습니다.

이것은 [이용허락규약\(Legal Code\)](#)을 이해하기 쉽게 요약한 것입니다.

[Disclaimer](#)

Thesis for the Degree of Master of Engineering

# The New Hybrid-dynamic Threshold Method for Sea-ice Detection using Himawari-8/AHI Data



by

Donghyun Jin

Department of Spatial Information Engineering

The Graduate School

Pukyong National University

February 2018

The New Hybrid-dynamic Threshold Method  
for Sea-ice Detection using Himawari-8/AHI  
Data

(Himawari-8/AHI 자료를 활용한  
새로운 Hybrid-dynamic Threshold 기법  
기반 해빙 탐지)

Advisor: Prof. Kyung-Soo Han

by  
Donghyun Jin

A thesis submitted in partial fulfillment of the requirements  
for the degree of

Master of Engineering in Department of Spatial Information Engineering,  
The Graduate School,  
Pukyong National University

February 2018


# The New Hybrid-dynamic Threshold Method for Sea-ice Detection using Himawari-8/AHI Data

A dissertation  
by  
Donghyun Jin


Approved by:



(Chairman) Prof. Han-Lim Lee



(Member) Prof. Jin-Soo Kim



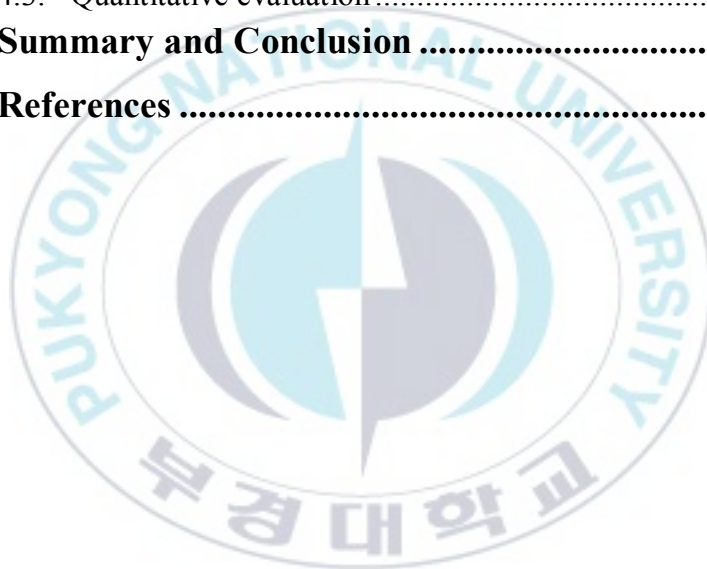
(Member) Prof. Kyung-Soo Han

February, 2018

# CONTENTS

<b>CONTENTS .....</b>	<b>i</b>
<b>LIST OF FIGURES .....</b>	<b>iii</b>
<b>LIST OF TABLES .....</b>	<b>vii</b>
<b>LIST OF ACRONYMS .....</b>	<b>viii</b>
<b>1. Introduction .....</b>	<b>1</b>
<b>2. Study area and data .....</b>	<b>7</b>
2.1. Study area .....	7
2.2. Study data .....	8
2.2.1. Satellite data .....	8
2.2.2. Validation data .....	18
<b>3. Sea-ice detection .....</b>	<b>20</b>
3.1. Overview .....	20
3.2. Building background data .....	22
3.2.1. Long-term satellite based sea-ice data .....	22
3.2.2. Snow spectral library .....	24
3.3. Pre-processing .....	26
3.3.1. Normalization using SZA data .....	27
3.3.2. Sea-ice candidate detection process .....	28
3.4. NDSI & 0.86 $\mu\text{m}$ reflectance test .....	29
3.5. Dynamic Wavelength Warping (DWW) method .....	34
3.5.1. DTW technique .....	34
3.5.2. DWW method .....	34
3.5.3. Input data .....	35
3.5.4. DWW algorithm process .....	36
3.5.5. Result on the DWW method .....	38
3.6. $\text{IST}_0$ test .....	40
3.6.1. Analysis using MODIS IST .....	40
3.6.2. $\text{IST}_0$ test .....	42

3.6.3. Result on $IST_0$ test.....	42
3.7. Ice re-check .....	44
3.8. Cloud re-check .....	47
3.8.1. Difference [Snow spectral library $R_{1.61\mu m}$ -Profile $R_{1.61\mu m}$ ] test.....	47
3.8.2. NDSI & BTD[11.0-3.8 $\mu m$ ] test.....	49
<b>4. Validation evaluation.....</b>	<b>52</b>
4.1. Validation strategy.....	52
4.2. Qualitative evaluation .....	55
4.3. Quantitative evaluation .....	58
<b>5. Summary and Conclusion .....</b>	<b>63</b>
<b>6. References .....</b>	<b>66</b>



# LIST OF FIGURES

Figure 1. Snow covered ice, new ice, water, cloud reflectance value depending on wavelength (George A. Riggs, et al., 1999). .....	3
Figure 2. Snow covered reflectance depending on Solar Zenith Angle (SZA). .....	3
Figure 3. The study area on this thesis. ....	8
Figure 4. Land/Sea mask on AHI FD map using 2013 MODIS land cover product. ....	13
Figure 5. NSIDC Northern Hemisphere EASE-Grid 2.0 Weekly sea-ice extent, 19810105-19810111. ....	14
Figure 6. MODIS Sea-ice product (MOD29). ....	17
Figure 7. VIIRS Sea-ice characterization (SWATH) product. ....	19
Figure 8. The flow chart on this algorithm ( $SZA < 80^\circ$ ). ....	21
Figure 9. Potential ice zone; Static boundaries depending on longitude and ice is also mapped on lakes in high-elevated areas in the Tibet region (Romanov P., 2016). ....	23
Figure 10. Long-term satellite based sea-ice data for 1966-2015 NSIDC Weekly snow and ice data. ....	24

Figure 11. Snow spectral library depending on wavelength and BTD...	26
Figure 12. Snow cover of visible reflectance before (a, b) and after correction (c, d) (COMS Algorithm Theoretical Basis Document, 2012).....	28
Figure 13. The sea-ice and ice-free water (No Sea-ice) histogram depending on 0.86 $\mu\text{m}$ reflectance.....	30
Figure 14. NDSI histogram of Sea-ice/Ice-free water.....	31
Figure 15. Comparison $R_{0.86\mu\text{m}}$ -NDSI image this algorithm, VIIRS sea-ice image and AHI RGB image.....	33
Figure 16. Two type of similarity and the warp path between time series, (a) shows the time-rigid similarity used by Euclidean distance ( $L_p$ ), (b) shows the time-flexible similarity by DTW, (c) shows warp path (green line) (Zhang et al., 2015).....	35
Figure 17. In case of warping path between snow spectral library and profile is fitting 1 to 1.....	37
Figure 18. Comparison DWW method image on this algorithm and AHI RGB image.....	39



Figure 19. Scatter plot for the relationship between T11 $\mu\text{m}$ and BTD[T11 $\mu\text{m}$ -T12 $\mu\text{m}$ ] according to IST 273.0 K or less (Jin <i>et al.</i> , 2017).....	41
Figure 20. Comparison IST <sub>0</sub> test image on this algorithm and AHI RGB image.....	43
Figure 21. The histogram for NDWI on sea-ice free(ice-free water) and sea-ice.....	45
Figure 22. Addition test to sea-ice pixel detected DWW and IST <sub>0</sub> test before (A) and after (B), (A-1, B-1, C-1) shows before, after and AHI RGB image on red box, (A-2, B-2, C-2) shows before, after and AHI RGB image on blue box, (C) shows before, after and AHI RGB image on yellow box.....	46
Figure 23. Comparison between AHI image applied cloud (left) and AHI RGB image (right).....	47
Figure 24. The difference [Snow spectral library R <sub>1.6 <math>\mu\text{m}</math></sub> – Profile R <sub>1.6 <math>\mu\text{m}</math></sub> ] histogram of sea-ice.....	48
Figure 25. Comparison NDSI-BTD test before(a), after(b) and RGB image(c).....	50

Figure 26. The sea-ice data using AHI channel data on this study. ....	51
Figure 27. (a) shows VIIRS SWATH sea-ice data, (b) shows VIIRS sea-ice data performed match-up on the Himawari8 observation area.	56
Figure 28. Comparison image between sea-ice algorithm and VIIRS sea-ice data (left side), AHI RGB image (right side), 20160112.0330 (UTC).....	60
Figure 29. Comparison image between sea-ice algorithm and VIIRS sea-ice data (left side), AHI RGB image (right side), 20160204.0300 (UTC).....	61
Figure 30. Comparison image between sea-ice algorithm and VIIRS sea-ice data (left side), AHI RGB image (right side), 20160220.0300 (UTC).....	62

## LIST OF TABLES

Table 1. MODIS IST Calculation Coefficients for Eq. 1 .....	5
Table 2. Himawari-08/AHI data which used by this study .....	10
Table 3. The MODIS Land cover IGBP type product Information .....	12
Table 4. Contingency table on this study .....	53
Table 5. Validation score compared with VIIRS sea-ice data; hit is sea-ice (both sea-ice algorithm and VIIRS sea-ice data, false is sea-ice on this algorithm and no sea-ice on VIIRS sea-ice data, miss is no sea- ice on this algorithm and sea-ice on VIIRS sea-ice data, correct- reject is no sea-ice (both this algorithm and VIIRS sea-ice data)..	58

## LIST OF ACRONYMS



ABI	Advanced Baseline Imager
AHI	Advanced Himawari Imager
BTD	Brightness Temperature Difference
CI	Comparison Index
DEM	Digital Elevation Model
DMSP	Defense Meteorological Satellite Program
DTW	Dynamic Time Warping
DWW	Dynamic Wavelength Warping
EDR	Environmental Data Record
FAR	False Alarm Ratio
FD	Full Disk
IGBP	International Geosphere-Biosphere Programme
IP	Intermediate Product
IST	Ice Surface Temperature
MODIS	Moderate Resolution Imaging Spectroradiometer
NDVI	Normalized Difference Vegetation Index
NDSI	Normalized Difference Snow Index

NOAA	National Oceanic and Atmospheric Administration
NSIDC	National Snow and Ice Data Center
POD	Probability of Detection
QA	Quality Assurance
SDS	Scientific Data Sets
SIC	Sea Ice Concentration
SMMR	Scanning Multichannel Microwave Radiometer
SSM/I	Special Sensor Microwave Imager
SSMIS	Special Sensor Microwave Imager/Sounder
SST	Sea Surface Temperature
SZA	Solar Zenith Angle
VIIRS	Visible Infrared Imager Radiometer Suite
VZA	Viewing Zenith Angle

# Himawari-8/AHI 자료를 활용한 새로운 Hybrid-dynamic Threshold 기법 기반 해빙 탐지

진 동 현

부 경 대 학 교 대 학 원 공 간 정 보 시 스템 공 학 과

## 요 약

해빙은 해수가 형상에 관계없이 동결하여 생성된 얼음으로서 적설로 덮인 얼음과 적설로 덮이지 않은 순수한 얼음으로 분포하며, 지표면 반사도 및 에너지 수지에 영향을 주는 등 지구의 기후시스템에 중요한 요소 중 하나이다. 또한 해빙은 고위도 및 극지방에 주로 분포하며 계절에 따른 변동성이 나타남으로 인해 인간이 직접 해빙을 관측하는 데는 한계가 있다. 이에 1960년대부터 현재까지 다양한 종류의 위성을 이용한 원격탐사를 통해 해빙탐지 연구가 활발히 진행되고 있으며, 특히 정지궤도 위성은 해빙의 지속적인 관측이 가능한 장점이 있다. 위성을 이용한 해빙탐지는 주로 위성의 가시영역 채널 반사도를 활용하는 기법과 Ice Surface Temperature (IST)를 활용한 기법을 통해 이루어진다. 그러나 해빙 중 적설로 덮인 얼음의 경우 적설로 덮이지 않은 얼음에 비해 태양 천정각 및 얼음의 상태에 따른 변동성이 높으며, IST 또한 대기 중 수증기, 밝기온도에 따른 IST 산출 계수의 불연속성으로 인해 두 기법을 이용할 경우, 잠재적인 오탐지 및 미탐지 가능성이 존재한다. 이에 본 연구에서는 정지궤도 위성인 Himawari-8에 탑재된 AHI 채널자료를 이용하여 적설로 덮인 얼음지역은 파장에 따른 반사도 변화패턴을 비교하는 Dynamic Wavelength Warping (DWW) 기법으로, 적설로 덮이지 않은 순수한 얼음지역은 IST 산출이 생략된 단순하고 효율적인 동적 임계치 기법을 통해 해빙을 탐지하였다. 본 연구에서 산출한 해빙자료의 정확도를 평가하기 위해 National Oceanic and Atmospheric Administration (NOAA)의 Visible Infrared Imager Radiometer Sensor (VIIRS) Sea-ice characterization 자료를 이용하였으며, 정량적 평가와 정성적 평가를 수행하였으며 정량적 평가 결과, Probability of Detection (POD)는 88.93 %, False Alarm Ratio (FAR)는

1.77 %로 높은 정확도를 보였다. 정성적 평가는 AHI RGB 영상과 함께 수행하였으며, 그 결과, VIIRS Sea-ice 자료는 구름과 해빙이 없는 바다가 혼재된 영역에 대해 해빙으로 오탐지하였으나, 본 연구에서 산출한 해빙 자료는 해당 영역을 오탐지하지 않았다.



# 1. Introduction

Sea-ice is ice arose by freezing open water regardless of its shape on the ocean. It is an important component of the earth's climate system because it affects the surface albedo and the thermal energy release of the oceans and regulates the exchange of water vapor · CO<sub>2</sub> · the gas between the ocean and the atmosphere (Allison *et al.*, 2014; Seo *et al.*, 2016). The sea-ice also has extent differently for season; about  $7.8 \times 10^6 \text{ km}^2$  in September with a minimum area of sea-ice, about  $20.0 \times 10^6 \text{ km}^2$  in March with a maximum area based on the northern hemisphere (Parkinson *et al.*, 1987). And in the case of sea-ice, it is distributed to widespread area on the earth, so it is difficult to approach human and there is variation with time such as variability depending on the season. Due to the characteristics of this sea-ice, from the 1960s, sea-ice was detected using satellite data, and sea-ice detection using satellite data is now actively being carried out. It is more temporal and spatial efficient than direct observation by human, many previous studies are using satellite data; Moderate Resolution Imaging Spectroradiometer (MODIS) onboard Terra/Aqua (Hall *et al.*, 2001), Visible Infrared Imaging Radiometer Suite (VIIRS) onboard Suomi-NPP (Key *et al.*, 2013), Advanced Baseline Imager (ABI) onboard GOES-R (Liu *et al.*, 2010). It is used in industrial areas such as shipping



and climate research such as sea-ice monitoring and utilized to calculate Sea Surface Temperature (SST), sea-ice information; thickness, extent, age. It divided into two methods on these day. One of methods is to use reflectance threshold method. It has been used single, multi-channel reflectance and Normalized Difference Snow Index (NDSI) to detect sea-ice (Hall *et al.*, 2001; Kawano and Kudoh, 2004; Liu and Key, 2010; Shi and Wang, 2012; Mahoney *et al.*, 2013). The Figure 1 is showed to reflectance of sea-ice, water, cloud depending on wavelength. Ice-free water is showed to confident difference from sea-ice. using the feature, we can discriminate between sea-ice and ice-free water. But what we should note in this Figure 1 is to show the difference in the reflectance new ice and snow covered ice. Despite these differences, the sea-ice detection method such as MODIS and VIIRS using reflectance has been detected sea-ice using a static threshold technique. In addition, such as the Figure 2, snow covered ice has had high variability depending on Solar Zenith Angle (SZA). Due to the variability of reflectance depending on SZA, sea-ice detection algorithms using a static threshold technique have potential false and miss detection.

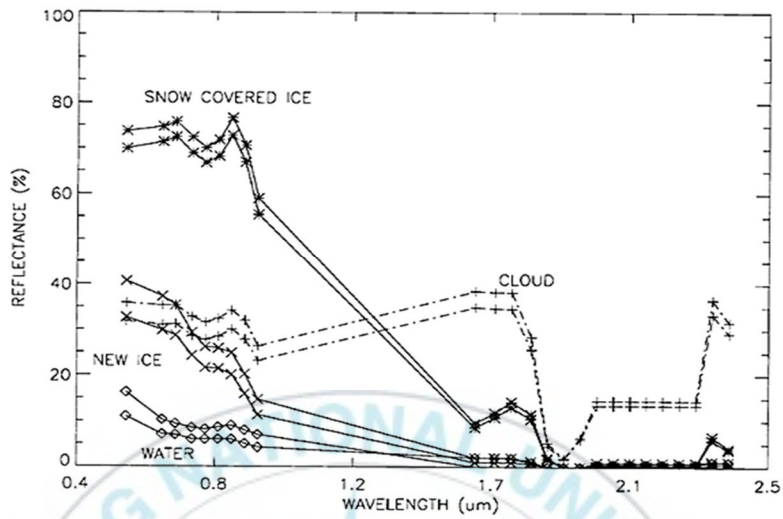


Figure 1. Snow covered ice, new ice, water, cloud reflectance value depending on wavelength (George A. Riggs, et al., 1999).

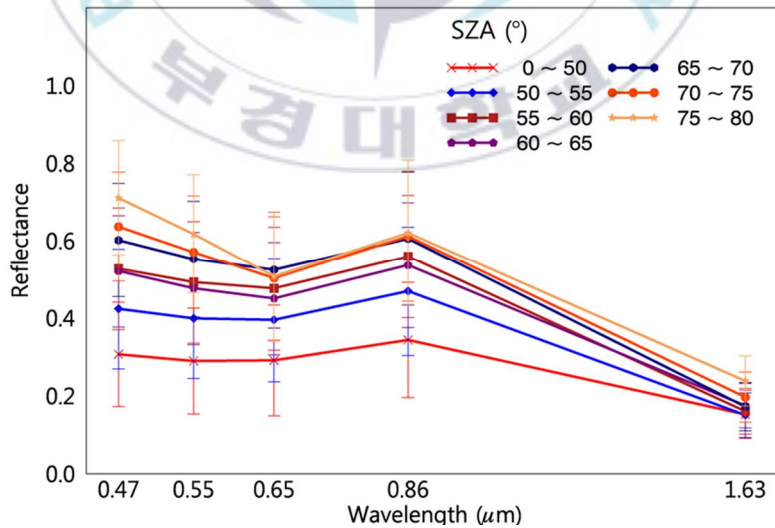


Figure 2. Snow covered reflectance depending on Solar Zenith Angle (SZA).

Another method is to use Ice Surface Temperature (IST) value. It was primarily introduced by Key *et al.* (1992) and it has been developed on these days, it has been actively researched for the detection of sea-ice. The MODIS IST is based on IST calculation method of the Key *et al.* (1997). The equation for calculating the MODIS IST is as follows.

$$IST = a + b \cdot BT_{11\mu m} + c \cdot (BT_{11\mu m} - BT_{12\mu m}) + d[(BT_{11\mu m} - BT_{12\mu m}) \cdot (\sec \theta - 1)] \quad \text{Equation 1}$$

- $BT_{11\mu m}$  : 11  $\mu m$  brightness temperature (K)
- $BT_{12\mu m}$  : 12  $\mu m$  brightness temperature (K)
- $\theta$  : Sensor scan angle from nadir
- a, b, c, d : empirically-determined coefficients for atmospheric effect, notably humidity

The above coefficients (a, b, c, d) are defined for temperature ranges of  $BT_{11\mu m}$  (~240 K, 240 K ~ 260 K, 260 K ~). The coefficients for IST calculation are showed to Table 1. They are calculated using the multiple linear regression method based on the snow age, topography, brightness temperature calculated from the atmospheric radiation model and other indices representing conditions such as humidity, wind. This complex

process must be preceded by each satellite sensor utilizing the IST for sea-ice detection. In addition, since this method has different values of the coefficient depending on the temperature ( $BT_{11\mu\text{m}}$ ), there is a potential error possibility in the IST continuity of the region when the coefficient is changed.

**Table 1. MODIS IST Calculation Coefficients for Eq. 1**

Temperature Range ( $BT_{11\mu\text{m}}$ )	a	b	c	d
< 240 K	-0.159480	0.999926	1.390388	-0.413575
240 – 260 K	-3.329456	1.012946	1.214573	0.131017
> 260 K	-5.207360	1.019429	1.510250	0.260355

Considering features of sea-ice, we have detected snow covered ice using Dynamic Wavelength Warping (DWW) based Dynamic Time Warping (DTW), a pattern change recognition technique. The DTW technique is an algorithm that determines the similarity of two temporally consecutive data according to a time series and has been adapted by Petitjean *et al.* (2012) for satellite image time series analysis. The DWW is a technique for determining the similarity using the change pattern of the

reflectance of two data according to wavelength instead of the time of DTW technique. Lee *et al.* (2017) was used DWW method for snow cover detection. It is strong point because it is a technique that utilizes the variability according to wavelength, not the static threshold method which is mostly used in the prior research and advanced institutions.

And considering bare ice detection, we used a simple and efficient method of using dynamic threshold value of 11  $\mu\text{m}$  brightness temperature instead of method using IST. Since the technique we used doesn't need IST calculation, the calculation process of IST coefficient was also not make use of. In case of dynamic threshold method to detect bare ice, we analyzed the correlation characteristics of MODIS IST  $\cdot$  Brightness Temperature Difference (BTD,  $BT_{11 \mu\text{m}} - BT_{12 \mu\text{m}}$ )  $\cdot$   $BT_{11 \mu\text{m}}$  and set threshold according to the correlation analysis result. Continuing, to evaluate the sea-ice detection technique proposed in this study, we compared and analyzed with VIIRS sea-ice data and Advanced Himawari Imager (AHI) RGB image.

## 2. Study area and data

### 2.1. Study area

We selected one of the representative areas where sea-ice is distributed to the Himawari-08/AHI measurement area. The Figure 3 shows study area. It is located at 29.69 ~ 65.29 N°, 114.61 ~ 170.55 E° and has been involved sea of Okhotsk. The sea of Okhotsk is located to the northwest Pacific, where sea-ice appears from December, and sea-ice is distributed in 70-80 % of a region in February. Therefore, previous many studies have used the sea of Okhotsk as a research area to carry out studies related to sea-ice (Cavalieri and Parkinson, 1987; Kimura and Wakatsuchi, 1999; Parkinson *et al.*, 1999; Jin *et al.*, 2017).

The temporal range of this study was selected from December ~ February 2015 ~ 2016, which is winter season on the northern hemisphere.



**Figure 3. The study area on this thesis.**

## **2.2. Study data**

### **2.2.1. Satellite data**

The channel data of the Himawari-08/AHI data is used to detect sea-ice. Ancillary data to perform this sea-ice detection algorithm is 2013 MODIS Landcover product for identifying land/sea. Training data is MODIS sea-ice extent product (MOD29\_L2), MODIS Snow Cover (MOD10\_L2) and National Snow and Ice Data Center (NSIDC) Weekly Snow cover and Sea-ice extent product to construct the necessary data in this algorithm. And validation data is VIIRS sea-ice characterization product.

### **2.2.1.1. Himawari-08/AHI data**

The Himawari-08 is the first in a series of next-generation geostationary satellite and AHI is weather imager onboard Himawari-08. It has 16-channel multi-spectral bands including six visible and near infrared and IR bands. The spatial resolution of AHI channel data consists of 500 m, 1 km, 2 km. These are different depending on each channel data. Detailed Information for AHI channel data we used is showed by Table 2. We will explain the availability of each channel data on Table 2.

The AHI instrument produces on Full-Disk (FD) image every 10-min and rapid scanning of Japan and target areas at 2.5-min intervals to sense the reflectance and emitted energy from the environment of the Asia-Pacific region. This study used channel data from FD format every 10-minute. And we used AHI data with cloud masking.



**Table 2. Himawari-08/AHI data which used by this study**

<b>Band</b>	<b>Center Wavelength [<math>\mu\text{m}</math>]</b>	<b>Spatial Resolution [km]</b>	<b>Availability</b>
<b>01</b>	0.4703	1 km	DWW processing input data, Rate ( $R_{1.61}/R_{0.47}$ ) test
<b>02</b>	0.5105	1 km	DWW processing input data
<b>03</b>	0.6399	500 m	DWW processing input data, NDSI test, Rate ( $R_{0.64}/R_{1.61}$ ) test, Selection cloud library
<b>04</b>	0.8563	1 km	Reflectance test, DWW processing input data, NDWI test
<b>05</b>	1.6098	2 km	Reflectance test, DWW processing input data, Difference [Snow spectral library $R_{1.61 \mu\text{m}} - R_{1.61 \mu\text{m}}$ ] test NDSI test, NDWI test
<b>07</b>	3.8848	2 km	DWW processing input data, BTD[ $BT_{11.2 \mu\text{m}} - BT_{3.8 \mu\text{m}}$ ] test
<b>14</b>	11.2432	2 km	DWW processing input data, BTD[ $BT_{11.2 \mu\text{m}} - BT_{3.8 \mu\text{m}}$ ] test, $IST_0$ test
<b>15</b>	12.3828	2 km	$IST_0$ test

### **2.2.1.2. MODIS Land cover**

We used MODIS land cover product to distribute land type before detecting sea-ice. It incorporates five different land cover classification schemes through a supervised decision-tree classification method. The primary land cover types identify 17 classes defined by the International Geosphere-Biosphere Programme (IGBP) (Belward et al., 1999; Scean, 1999; Friedl et al., 2002; Fiedl et al., 2010); including 11 natural vegetation classes, three human-related classes, and three non-vegetation classes. This product of data type is un-sign 1-byte integer.

The MODIS land cover type product supplies global maps of land cover on every year from 2001 to 2013 and this study used 2013 MODIS land cover product.

The map projection type of its product is provided to sinusoidal tile grid map type and 500 m spatial resolution. On the other hand, as our study area is geostationary projection map type, we performed match-up from sinusoidal tile grid map to geostationary.

The Table 3 shows MODIS land cover IGBP type index information. We distribute to ocean using MODIS land cover IGBP type index.

The Figure 4 shows land/sea mask using 2013 MODIS land cover on geostationary projection map type.

Table 3. The MODIS Land cover IGBP type product Information

<b>Data value</b>	<b>IGBP Type</b>	<b>Characteristic</b>
0	Water	Non-vegetated class
1	Evergreen Needleleaf forest	
2	Evergreen Broadleaf forest	
3	Deciduous Needleleaf forest	
4	Deciduous Broadleaf forest	
5	Mixed forest	
6	Closed shrublands	Natural vegetation class
7	Open shrublands	
8	Woody savannas	
9	Savannas	
10	Grasslands	
11	Permanent wetlands	
12	Croplands	
13	Urban and built-up	Human-altered class
14	Cropland/Natural vegetation mosaic	
15	Snow and ice	Non-vegetated class
16	Barren or sparsely vegetated	
254	Unclassified	-
255	Fill Value	-

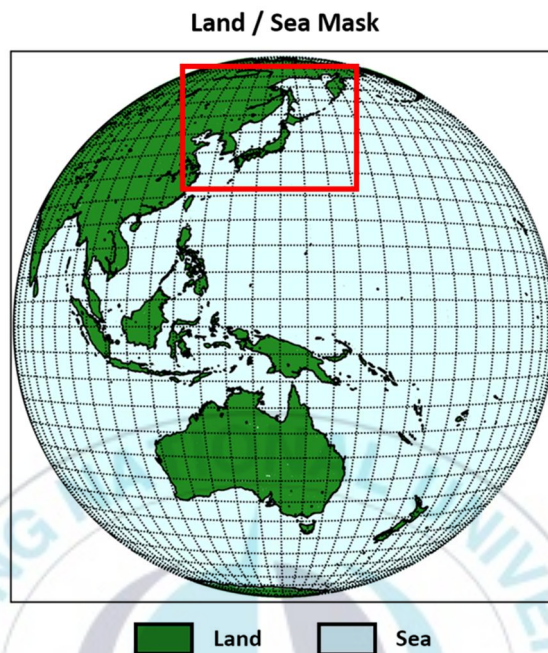


**Figure 4. Land/Sea mask on AHI FD map using 2013 MODIS land cover product.**

### **2.2.1.3. NSIDC Weekly Snow cover and Sea-ice extent product**

NSIDC weekly snow cover and sea-ice extent product consist of snow cover and sea-ice information and we used only sea-ice information. The sea-ice information is made by the sea-ice concentrations from Nimbus-7 Scanning Multichannel Microwave Radiometer (SMMR) and Defense Meteorological Satellite Program (DMSP) Special Sensor Microwave Imager (SSM/I) – Special Sensor Microwave Imager/Sounder (SSMIS) passive microwave data. When sea-ice concentration is greater than 15

percent in a majority of a given week's sea-ice files. The 15 percent ice concentration isopleth is a conventionally accepted cutoff for the ice edge (Johannessen *et al.*, 2004). The spatial coverage of its data is northern hemisphere and spatial resolution is 25 km. The temporal coverage of its data is from 23 October 1966 through 25 December 2015 and temporal resolution is weekly. A week is defined as seven days.

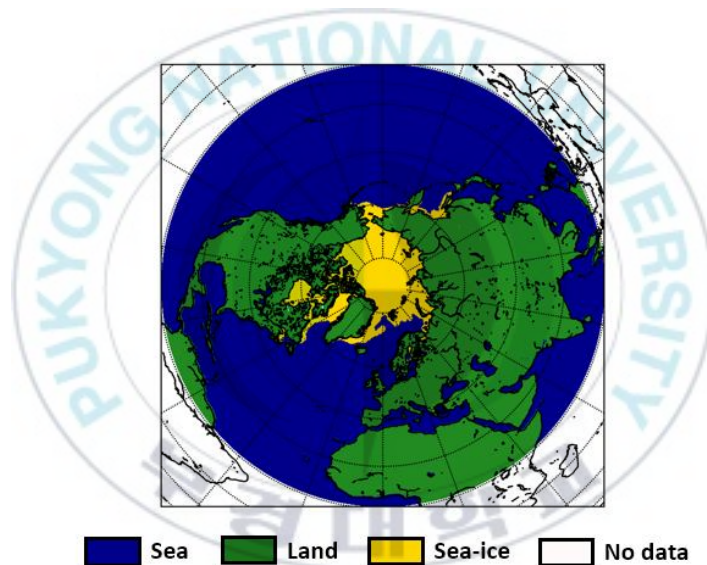


**Figure 5. NSIDC Northern Hemisphere EASE-Grid 2.0 Weekly sea-ice extent, 19810105-19810111.**

#### **2.2.1.4. MODIS Snow cover product**

The MODIS snow cover product is generated using the MODIS calibrated radiance data product (MOD02HKM), the geolocation product

(MOD02), and the cloud mask product (MOD35\_L2) as inputs. The MODIS snow cover algorithm (MOD10\_L2) contains Scientific Data Sets (SDS) of snow cover, Quality Assurance (QA) SDSs, latitude and longitude SDSs, local attributes and global attributes. The snow cover algorithm identifies snow-covered land; it also identifies snow-covered ice on inland water. The accuracy of the MODIS snow extent product varies with land-cover type, but overall, the accuracy under clear sky conditions has been assessed at 92 % in various peer-reviewed publications. The overall absolute accuracy of the well-studied 500 m resolution swath (MOD10\_L2) and daily tile (MOD10A1) products is ~93 %.

#### **2.2.1.5. MODIS Sea-ice extent product**

The MODIS sea-ice extent product is made by MODIS instruments onboard Terra/Aqua satellites and have been produced by MODIS channel data (MOD021KM), MODIS geolocation data (MOD03) and MODIS cloud mask product (MOD35\_Swath). It is designed to identify the presence of sea-ice in each 1 km pixel swath and to calculate the IST. The temporal resolution of its product is 5-min.

This product is used as validation and comparison data in many studies such as Gignac *et al* (2017). This study used MOD29 data as training data.

Maps of ice extent and IST in MOD29 under clear skies have RMS errors of 1.2-1.3 K during the “cold months” or when there is no surficial melt on the sea-ice.



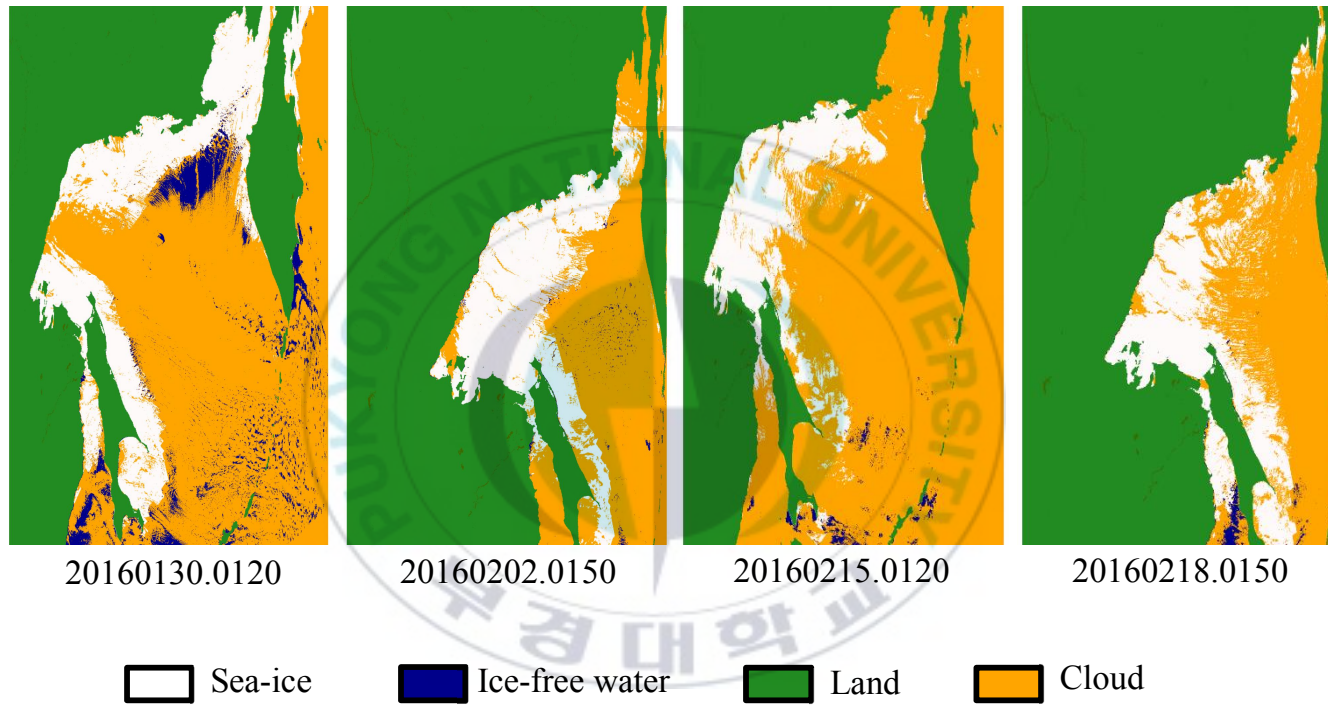


**Figure 6. MODIS Sea-ice product (MOD29).**



## **2.2.2. Validation data**

### **2.2.2.1. VIIRS Sea-ice characterization product**

The VIIRS Sea Ice Characterization (SIC) Environmental Data Record (EDR) uses the VIIRS SIC Intermediate Product (IP) as a primary input. The SIC EDR is an ice age classification map that contains classifications for ice-free, New/Young Ice and all other ice categories. New/Young ice has a maximum thickness of 30 cm, while All other ice is thicker than 30 cm. The algorithm has a daytime (reflectance threshold) branch and a night-time (energy balance) branch. The night-time algorithm does not utilize albedo as input, relying more on the IST EDR to determine ice growth and subsequent thickness. The Figure 7 is 3 scenes of the VIIRS sea-ice product. Each scene has black stripes as it moves away from nadir. This is caused by eliminating the overlapping area of several pixels when the Viewing Zenith Angle (VZA) is more than 32.0 degree in order to attenuate the “bow-tie effect”, which the image is distorted as it moves away from the nadir.

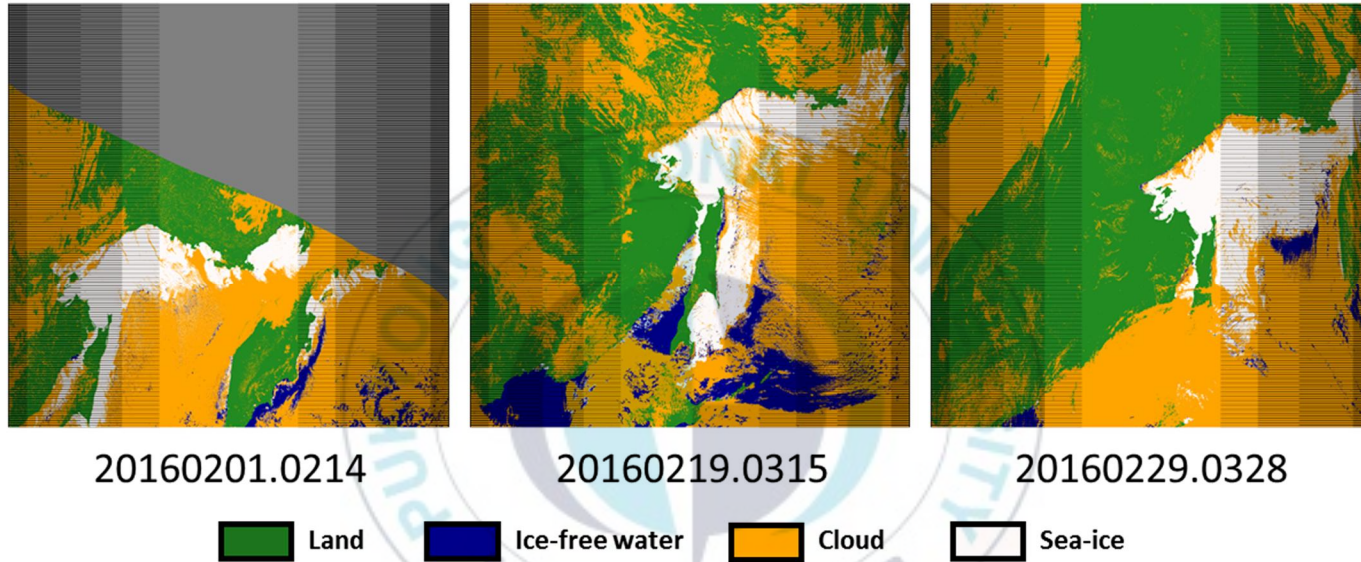


Figure 7. VIIRS Sea-ice characterization (SWATH) product.

## 3. Sea-ice detection

### 3.1. Overview

The sea-ice detection algorithm in this paper is divided into five processes. Before performing sea-ice detection algorithm, we constructed ancillary data for this study. The first step of this algorithm is pre-processing before sea-ice detection. Next step is to distinguish between confident sea-ice and ice-free water. After detecting confident sea-ice and ice-free water, considering snow covered ice, we used DWW technique to extra pixel. And we used dynamic threshold method (step 3). Last step is cloud/ice re-check. The Figure 8 is flow chart on this algorithm.

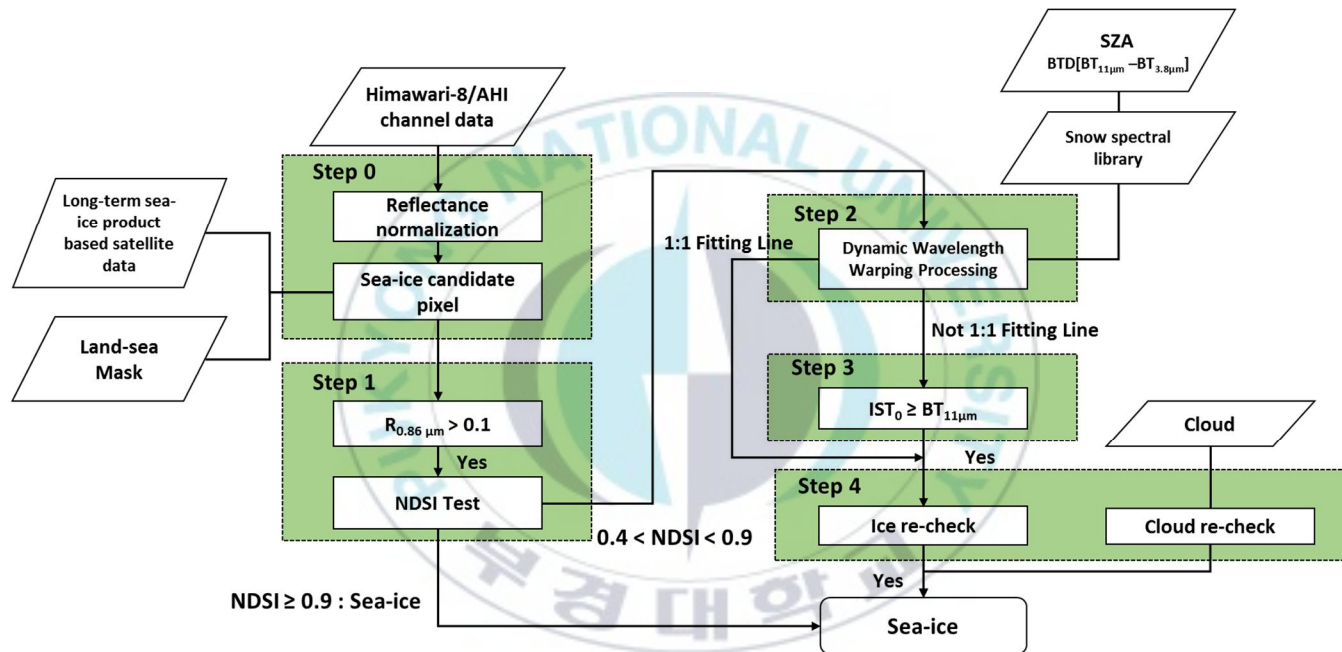


Figure 8. The flow chart on this algorithm (SZA < 80 °).

## **3.2. Building background data**

### **3.2.1. Long-term satellite based sea-ice data**

The sea-ice has been placed in high latitude area and polar region. In other words, the sea-ice is distributed in the specific ocean and regions. In this reason, many studies for sea-ice detection have used to set the sea-ice candidate zone, mainly using latitude data. The setting method using latitude data is used by recent studies commonly on these day. As more detailed, it is set a sea-ice candidate area using latitude depending on longitude. Although this method is easy and simple, the region where the sea-ice is presented until now is set as the sea-ice candidate region as shown in Figure 9. This feature has potential sea-ice false detection possibility. So, in this study, to set accurate sea-ice candidate region, we constructed and used long-term satellite based sea-ice data. It used NSIDC weekly snow cover and sea-ice extent product for 50 years. To increase the accuracy of the potential sea-ice area, we have collected more than 50 years of data and set the sea-ice area as an area of sea-ice if there is at least on sea-ice for 50 years (Figure 10 (a)). And as this process is just to determine sea-ice candidate region, we performed to extend a sea-ice candidate region. If certain pixel is sea-ice candidate, we extended 50 by 50 pixel to sea-ice candidate region around certain pixel. The Figure 10 (b) is shown

to long-term satellite based sea-ice data. However, since the NSIDC data is a polar stereographic map projection, it differs from the map projection, which is a geostationary map type. For this reason, it was necessary to match-up NSIDC data with AHI map type. In this study, distance was calculated using NSIDC geolocation data and AHI geolocation data, and the pixel with the minimum distance was determined as the closest pixel. Through this process, we matched the NSIDC data to the AHI map projection.

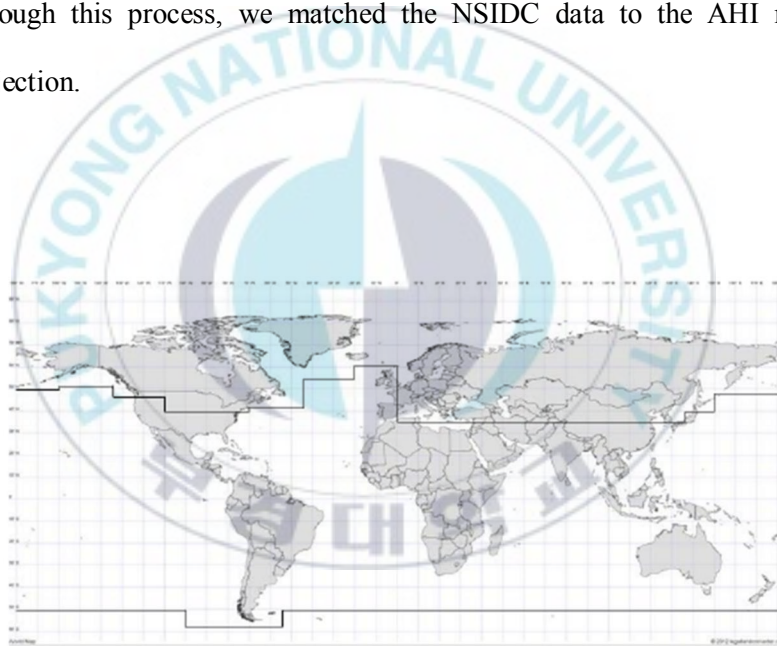


**Figure 9. Potential ice zone; Static boundaries depending on longitude and ice is also mapped on lakes in high-elevated areas in the Tibet region (Romanov P., 2016).**

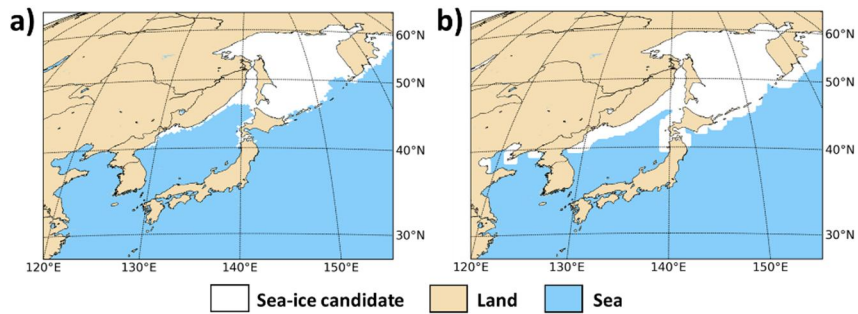


**Figure 10. Long-term satellite based sea-ice data for 1966-2015 NSIDC Weekly snow and ice data.**

### 3.2.2. Snow spectral library

The snow spectral library is made to use Dynamic Wavelength Warping (DWW) process. The DWW process needs two data. One data is snow standard data, another data is reflectance and BTD [ $BT_{11.0\ \mu\text{m}} - BT_{3.8\ \mu\text{m}}$ ] on the sea-ice candidate pixel. We defined another data to spectral profile. This part is to explain a standard data.

The sea-ice region is divided into two types. One type of sea-ice is snow covered sea-ice and another type is bare ice. Although snow covered ice region resembles to bare ice region, these regions have still difference characteristics. One feature is albedo value. The snow covered ice region

is higher than bare ice region (Figure 1). So, we divided into two type on sea-ice and the DWW technique is used to detect snow covered ice region.

The snow covered ice has same feature with snow cover. Because of this feature, we need snow standard data and MODIS Snow cover (MOD10\_L2) product has been used in many recent studies and very useful as snow cover standard data. Collected period is from December 2015 to February 2016. We obtained 2,636,900 snow pixels using the MODIS data collected during this period. To build snow spectral library, it needs nine type information on snow pixel. Nine type information are SZA, Digital Elevation Model (DEM), AHI channel No. 1 to 5 (0.46, 0.51, 0.64, 0.86, 1.61  $\mu\text{m}$ ), No. 7(3.8  $\mu\text{m}$ ) and 14(11.0  $\mu\text{m}$ ) data. The snow covered ice has different reflectance and BTD [ $BT_{11.0 \mu\text{m}} - BT_{3.8 \mu\text{m}}$ ] value depending on SZA and DEM of the snow covered ice region has low value. Another feature is BTD. The BTD on snow pixel is distribute -70.0 to 20.0. but reflectance range is 0.0 to 1.0. In this feature, we need to normalize between BTD and reflectance value and converted BTD range to 0.0 ~ 1.0. In this process, we called to BTD normalization. Its equation is shown to Equation 2.



### BTD Normalization

$$= \frac{BTD \text{ value} - BTD \text{ Min.} (-70.0)}{BTD \text{ Max.} (20.0) - BTD \text{ Min.} (-70.0)} \quad \text{Equation 2}$$

Using these features, when DEM is 0 ~ 500 m, we build to seven snow spectral library depending on SZA using reflectance and BTD normalization. The Figure 11 is shown snow spectral library.

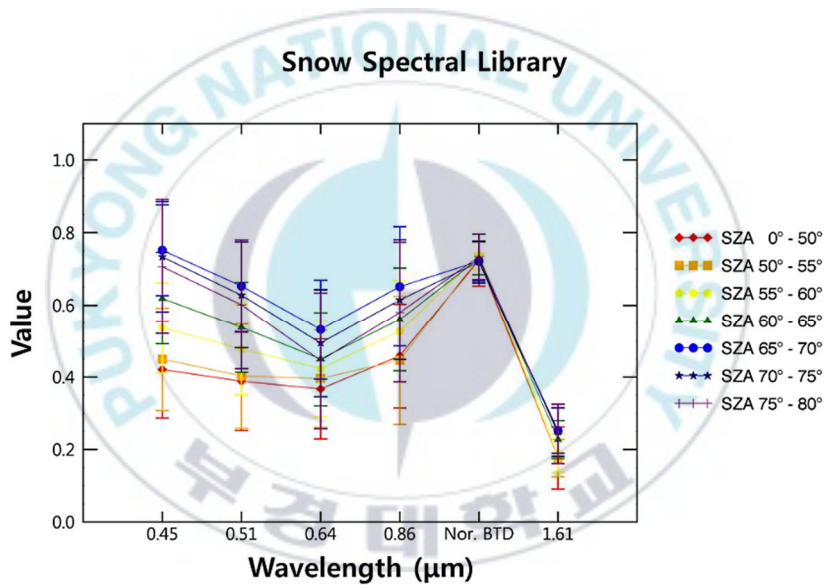


Figure 11. Snow spectral library depending on wavelength and BTD.

### 3.3. Pre-processing

This paper has two pre-processing before sea-ice detection algorithm. First, the reflectance of visible wavelength range has been affected by SZA.

In that case, we performed to normalize visible wavelength reflectance data. Second, we used land/sea mask and long-term satellite based sea-ice data to discriminate sea-ice candidate pixel.

### 3.3.1. Normalization using SZA data

The SZA of the sea-ice varies with local time and the AHI has observed the same. This is because that AHI is mounted on geostationary satellite; i.e., AHI visible range reflectance is affected by the SZA. The visible-range channel reflectance of the same sea-ice area is subject to variation over time. The higher the SZA value, the lower the reflectance of the observed visible channel (Barker and Strahler, 1993).

The Normalization of channel reflectance using SZA is shown in Equation 3.

$$\rho' = \frac{\rho}{\cos(SZA)}$$

Equation 3

$\rho$  is the channel reflectance and  $\rho'$  is the normalized channel reflectance using the SZA. The Figure 2 shows the reflectance pattern variation of sea-ice with wavelength before and after the reflectance normalization of each channel. Before normalization, a higher SZA yields a lower reflectance

(Figure 12 a, b), while after normalization, reflectance is similar among different SZA values (Figure 12 c, d).

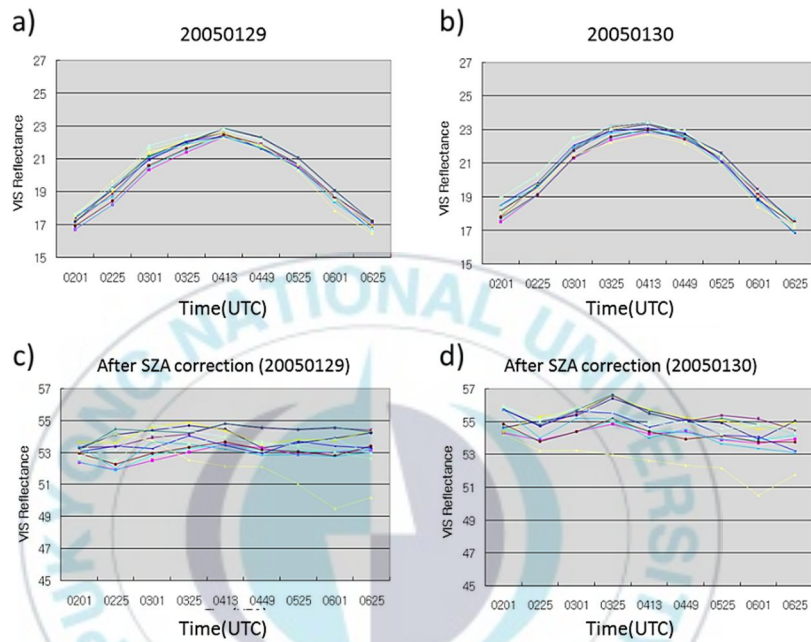


**Figure 12. Snow cover of visible reflectance before (a, b) and after correction (c, d) (COMS Algorithm Theoretical Basis Document, 2012).**

### 3.3.2. Sea-ice candidate detection process

This process is simple test using two types data. One data is land/sea mask. It is used to distinguish between land and sea. Another data is long-term satellite based sea-ice data. The data presented above were constructed using over 50 years of sea-ice data, which are of climatic

significance. Since the area of this study is a part of the northern hemisphere including the sea of Okhotsk, this data was also utilized only in the northern hemisphere. Through these two processes, we classified the candidate sea-ice pixels.

### **3.4. NDSI & 0.86 $\mu\text{m}$ reflectance test**

In case of sea-ice or cloud-free ocean, the energy due to moisture is much absorbed on ocean, so very low reflectance is observed ice-free water at 0.86  $\mu\text{m}$  compared to sea-ice or cloud. The Figure 13 shows a histogram of 0.86  $\mu\text{m}$  observed in ice-free water and sea-ice. As in previous studies, it has low reflectance in the ice-free water and high reflectance sea-ice. Using these characteristics, this test could classify the sea-ice candidate as 0.86  $\mu\text{m}$  or less 0.1 or more sea-ice candidate pixel.

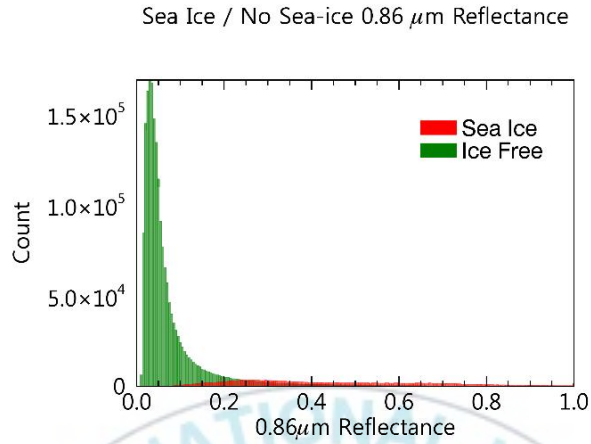


**Figure 13. The sea-ice and ice-free water (No Sea-ice) histogram depending on 0.86  $\mu\text{m}$  reflectance.**

The NDSI is useful for the detection of snow and sea-ice and for separating snow/sea-ice and most clouds. The NDSI is a calculation of the relative value of the characteristic reflectance difference between the visible and short-wave IR reflectance of snow/sea-ice. The NDSI is analogous to the normalized-difference vegetation index (NDVI) (Tucker, 1979). For Equation 4 is followed as:

$$\text{NDSI} = \frac{R_{0.64 \mu\text{m}} - R_{1.61 \mu\text{m}}}{R_{0.64 \mu\text{m}} + R_{1.61 \mu\text{m}}} \quad \text{Equation 4}$$

Pure snow/sea-ice has a high NDSI but NDSI decreases as other features are mixed in a pixel. Snow/Sea-ice in mixed pixels has an NDSI

that is less than pure snow/sea-ice. Pure snow/sea-ice can be distinguished by NDSI value.

The Figure 14 shows a histogram of NDSI observed in ocean and sea-ice. Using features, we set the threshold. If NDSI is over 0.9, we discriminate confidently sea-ice. If NDSI is lower 0.4, we discriminate no sea-ice pixel.

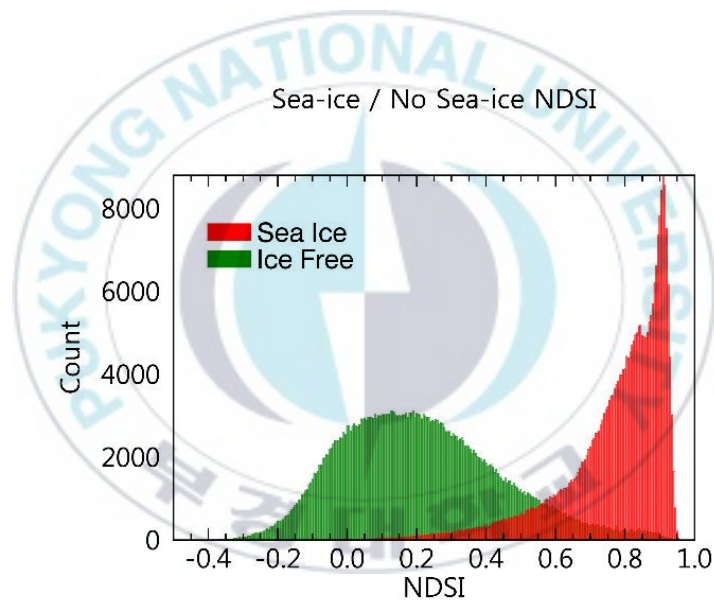


**Figure 14. NDSI histogram of Sea-ice/Ice-free water.**

As result of applying 0.86  $\mu\text{m}$  reflectance and NDSI test, it showed 99.6119 % accuracy when compared with VIIRS sea-ice product.

In case of comparison with AHI RGB image, ice-free water pixel classified by this test is judged to be well detected when compared with AHI RGB image. And “a” area of Figure 15 shows step 1 ice pixel. Comparing with RGB image, we judged to be well detected sea-ice.



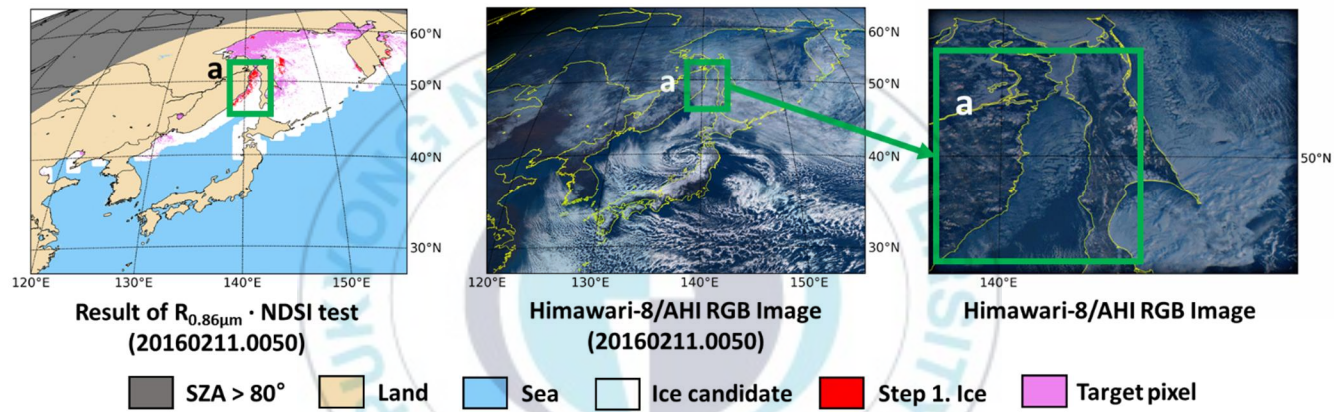


Figure 15. Comparison  $R_{0.86\mu\text{m}} \cdot \text{NDSI}$  image this algorithm, VIIRS sea-ice image and AHI RGB image.



## **3.5. Dynamic Wavelength Warping (DWW) method**

### **3.5.1. DTW technique**

The DWW method is based on DTW process. This approach can also be used to identify the optimal difference between two time-dependent data series, and the algorithm finds the similarity with the least cumulative cost, called the warp path (Keogh and Pazzani, 2001), using a shortest path algorithm which starts at the last pair and works back to the first pair. The commonly used cost is a quantitative measure of the similarity or difference between two points. To better explain the inner workings of the algorithm and its components, this part first describes the DWW method. Next, we explained to input data on DWW method and the algorithm is explained step-by-step with illustrative elements which help to explain each component in the algorithm.

### **3.5.2. DWW method**

This study used the DWW method with wavelength instead of time to track changes in the reflectance pattern. In this research, we used the DWW technique to detect the snow covered ice between snow library and data on sea-ice candidate pixel. The snow covered ice is same feature to snow

cover. Based on this fact, we used DWW method to detect snow covered ice.

### 3.5.3. Input data

The DWW method is based on the idea of measuring the similarity of distance between two elements; snow spectral library(X) and AHI channel data(Y). This is usually performed using a metric, such as the generalized norm, or  $L_p$  distance (Euclidean distance). The cost  $C(i,j)$  of mapping two points  $(X_i, Y_j)$  together is based on this calculated distance from the input wavelength and BTD data sets X and Y.

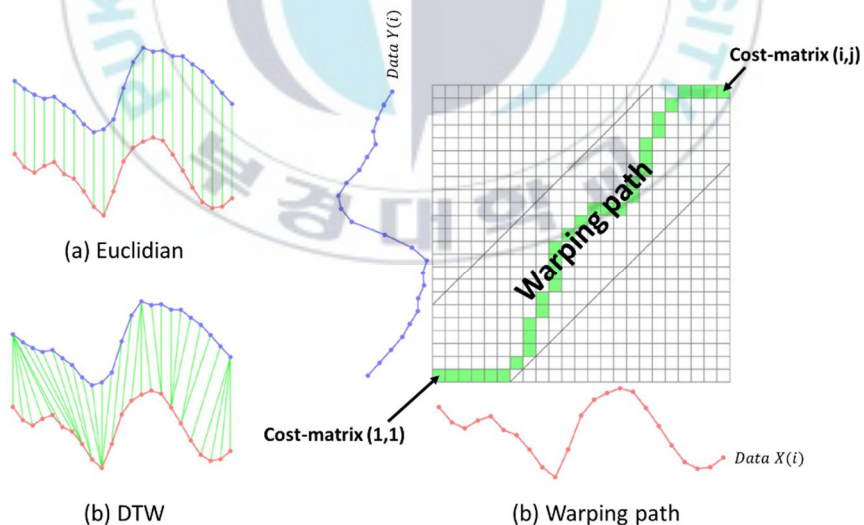


**Figure 16. Two type of similarity and the warp path between time series, (a) shows the time-rigid similarity used by Euclidean distance ( $L_p$ ), (b) shows the time-flexible similarity by DTW, (c) shows warp path (green line) (Zhang et al., 2015).**

### 3.5.4. DWW algorithm process

DWW method detailed process is follow as.

Firstly, It progress to calculate cost-matrix point (1,1).

- Calculating the Euclidean distance ( $L_p$ ) of each norm (Equation 5)

$$L_p(i, j) = \sqrt{(A_i - B_j)^2} \quad \text{Equation 5}$$

- Cost matrix of (1,1) ( $G$ ) is equal to the Euclidean distance of the (1,1) (Equation 6)

$$G(1, 1) = L_p(1, 1) \quad \text{Equation 6}$$

- Calculate the cost matrix in row 1 (Equation 7)

$$G(i, 1) = G(i - 1, 1) + L_p(i, 1) \quad (i = 1, m) \quad \text{Equation 7}$$

- Calculate the cost matrix in column 1 (Equation 8)

$$G(1, j) = G(1, j - 1) + L_p(1, j) \quad (j = 1, m) \quad \text{Equation 8}$$

- Calculate the cost matrix from left to right and from bottom to upon in column from 2 to m (Equation 9)

$$G(i, j) = \min[G(i, j - 1), G(i - 1, j), G(i - 1, j - 1)] + L_p(i, j) \quad \text{Equation 9}$$

- Find the minimum value of the path decision cost matrix from  $G(m, m)$

Find the minimum value of the path decision cost matrix from  $G(m, m)$ . The tracking path to find the minimum value is the warping path. The warping path shows the similarity between the snow library and AHI data. If warping path is 1 to 1, that pixel is snow covered ice (Figure 17) and if warping path is not 1 to 1, that pixel performs the next step.

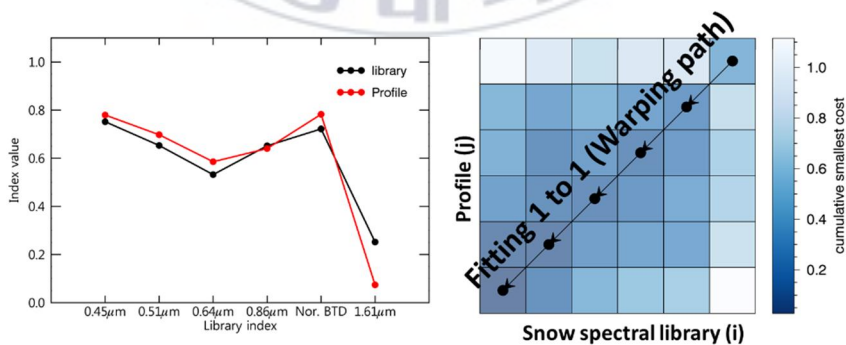


**Figure 17. In case of warping path between snow spectral library and profile is fitting 1 to 1.**

### 3.5.5. Result on the DWW method

The result of DWW method is shown in Figure 18. VIIRS which is validation data on this study have not been provided snow covered ice information and no data on sea-ice product by satellite data. In this reason, we compared simply our output with AHI RGB image. The comparison result is high concordance rate on sea-ice and ice-free water.



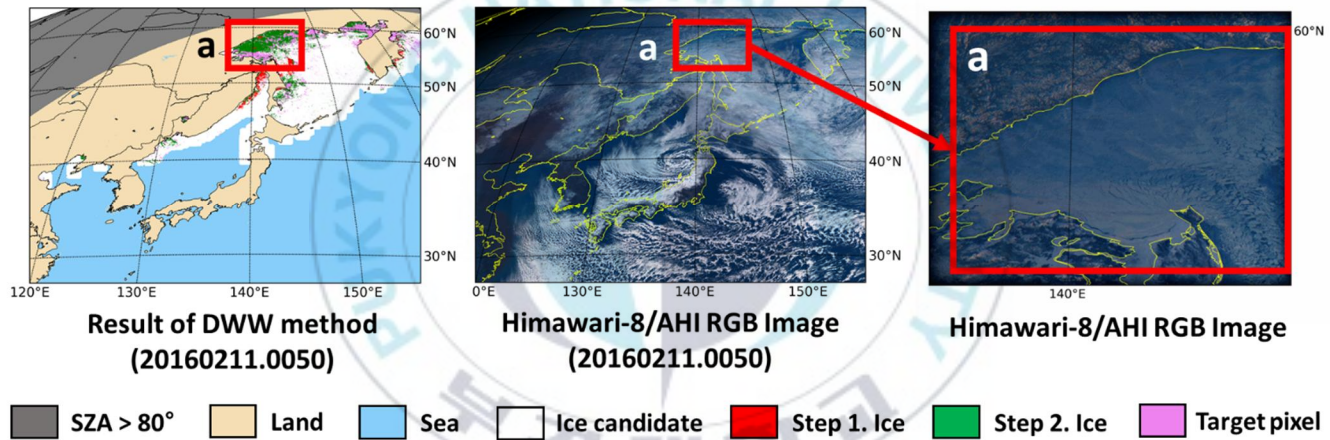


Figure 18. Comparison DWW method image on this algorithm and AHI RGB image.

### 3.6. IST<sub>0</sub> test

On the clear sky condition, sea-ice detection method using IST have potential error possibility due to IST calculation coefficients. Because of discontinuity of IST coefficient depending on atmospheric condition,  $T_{11 \mu\text{m}}$ , and so on, IST has difference between real-IST data and calculated IST. Therefore, we propose a simple and efficient sea-ice detection technique that omits IST calculation.

#### 3.6.1. Analysis using MODIS IST

In the case of clouds, it is one of the major error factors of satellite-based sea-ice detection as the similar characteristics of sea-ice and optical properties. Therefore, in this study, we selected the training scene using MODIS sea-ice extent and RGB image to perform accurate analysis of sea-ice. To understand the characteristics of sea-ice, the correlation between MODIS IST,  $BT_{11 \mu\text{m}}$  and BTD [ $BT_{11 \mu\text{m}} - BT_{12 \mu\text{m}}$ ] was performed on selected scenes. MODIS IST was calculated using the method of Hall *et al.* (2001), and MODIS band 31 (11  $\mu\text{m}$ ) and 32 (12  $\mu\text{m}$ ) channel data were extracted for the pixels whose calculated MODIS IST was 273.0 K or less, which is the freezing point of sea-water and converted from channel

data to brightness temperature using scale factor and offset value. BTD was also analyzed to take into account the water vapor effect, which is one of the error factors in detecting sea-ice. According to the interrelation of three values (MODIS IST,  $BT_{11 \mu\text{m}}$ , BTD), the relationship between  $BT_{11 \mu\text{m}}$  and BTD according to MODIS IST was linear. To understand the effect of  $BT_{11 \mu\text{m}}$  and BTD according to MODIS IST, further analysis was performed by classifying MODIS IST (271.0–271.5 K, 271.5–272.0 K, 272.0–272.5 K, and 272.5–273.0 K) value at 4.0 K interval. As a result of further analysis, the relationship between  $BT_{11 \mu\text{m}}$  and BTD according to the classified MODIS IST section also showed linear features (Figure 19).

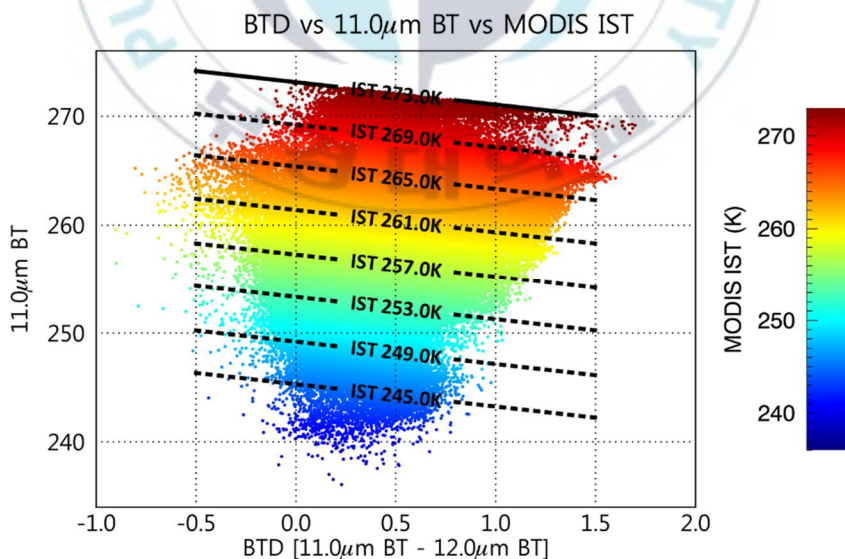


**Figure 19. Scatter plot for the relationship between  $T_{11 \mu\text{m}}$  and  $\text{BTD}[T_{11 \mu\text{m}} - T_{12 \mu\text{m}}]$  according to IST 273.0 K or less (Jin *et al.*, 2017).**



### 3.6.2. $IST_0$ test

From the analysis result, MODIS IST sets the line having the maximum value per MODIS IST range as the reference line, and sets the set reference line as the threshold value. In this study, sea-ice was detected by using the threshold of solid line in the upper part line of the IST range (269.0-273.0 K). The specified threshold value is defined as  $IST_0$ , and the equation to obtain it is as follows.

$$IST_0 = a \cdot \text{BTD} [T_{11 \mu\text{m}} - T_{12 \mu\text{m}}] + b \quad \text{Equation 10}$$

In the Equation 10, the coefficient a is -2.056, the coefficient of b is 273.1, and  $IST_0$  calculated by substituting each coefficient and BTD into the equation means  $BT_{11 \mu\text{m}}$  where MODIS IST is 273.0 K. In this study, sea ice was detected when  $BT_{11 \mu\text{m}}$  was less than  $IST_0$ .

### 3.6.3. Result on $IST_0$ test

The result of  $IST_0$  test is shown in Figure 20. On the clear sky condition, the test is well-done performance to detect bare ice compared with AHI RGB image.

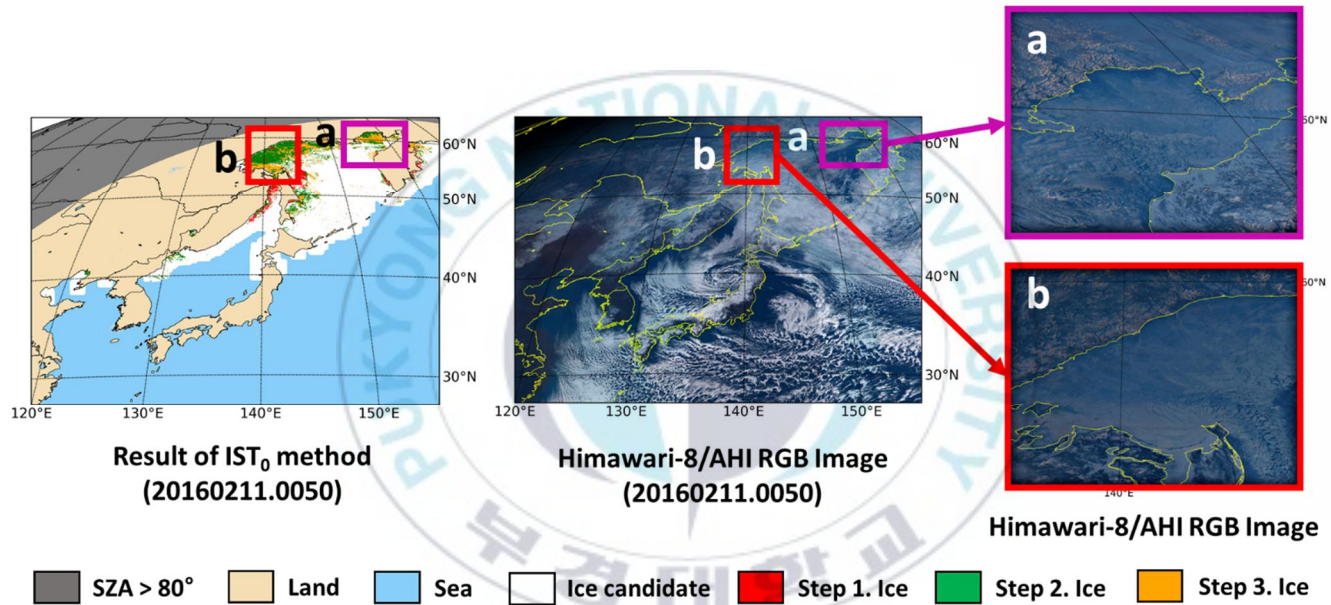


Figure 20. Comparison IST<sub>0</sub> test image on this algorithm and AHI RGB image.

### 3.7. Ice re-check

Although both test are high performance to detect sea-ice, they are tend to over-detect a sea-ice pixel using DWW and  $IST_0$  method. In this reason, we performed additionally to discriminate no ice from detected sea-ice pixel. The  $0.86 \mu\text{m}$  reflectance-NDSI-NDWI test are performed only on sea-ice pixels separated by DWW method and  $IST_0$  test.

The Normalized Difference Water Index (NDWI) is method that has been developed to delineate open water features and enhance their presence in remotely-sensed imagery. Previous studies have shown the NDWI can be used for semi-automatic glacier lake detection (Huggel, 1998; Huggel *et al.* 2002; Paul, 2007) and it is used to detect slush, open water (Bell *et al.*, 2017). The Equation 11 below is to obtain NDWI.

$$\text{NDWI} = \frac{R_{0.86 \mu\text{m}} - R_{1.61 \mu\text{m}}}{R_{0.86 \mu\text{m}} + R_{1.61 \mu\text{m}}} \quad \text{Equation 11}$$

This process has three test. One test is  $0.86 \mu\text{m}$  reflectance test. If its value is lower 0.15, the pixel is discriminated to ice-free water pixel. Another test is NDSI test. If its value is lower 0.4, the pixel is discriminated

to ice-free water. Last test is NDWI test. If its value is lower 0.45, the pixel is discriminated to ice-free water (Figure 21).

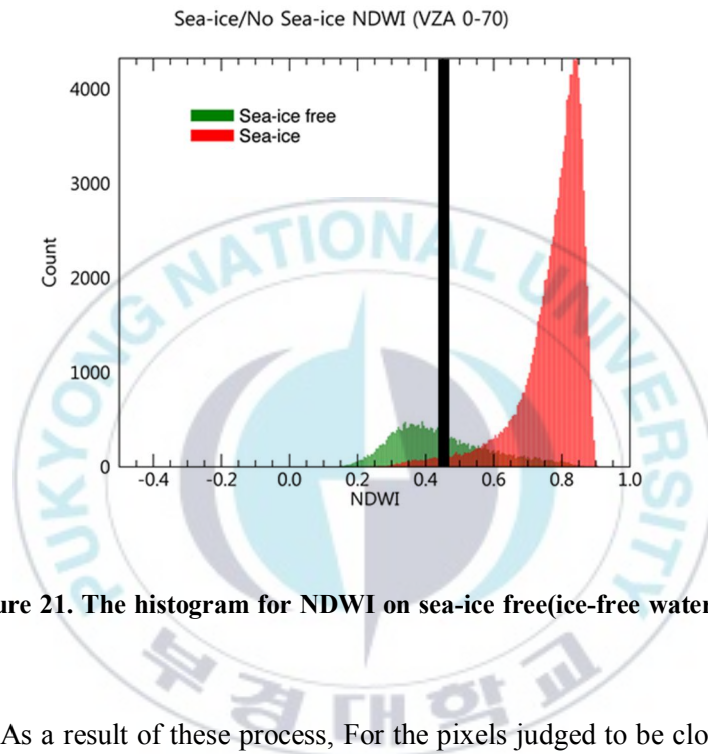


**Figure 21.** The histogram for NDWI on sea-ice free(ice-free water) and sea-ice.

As a result of these process, For the pixels judged to be clouds in the AHI RGB image, we classified them into pixels, not sea-ice, in this algorithm. In addition, the area that was detected by sea-ice near the boundary between the cloud and the ice-free water was also divided into pixels, not sea-ice.

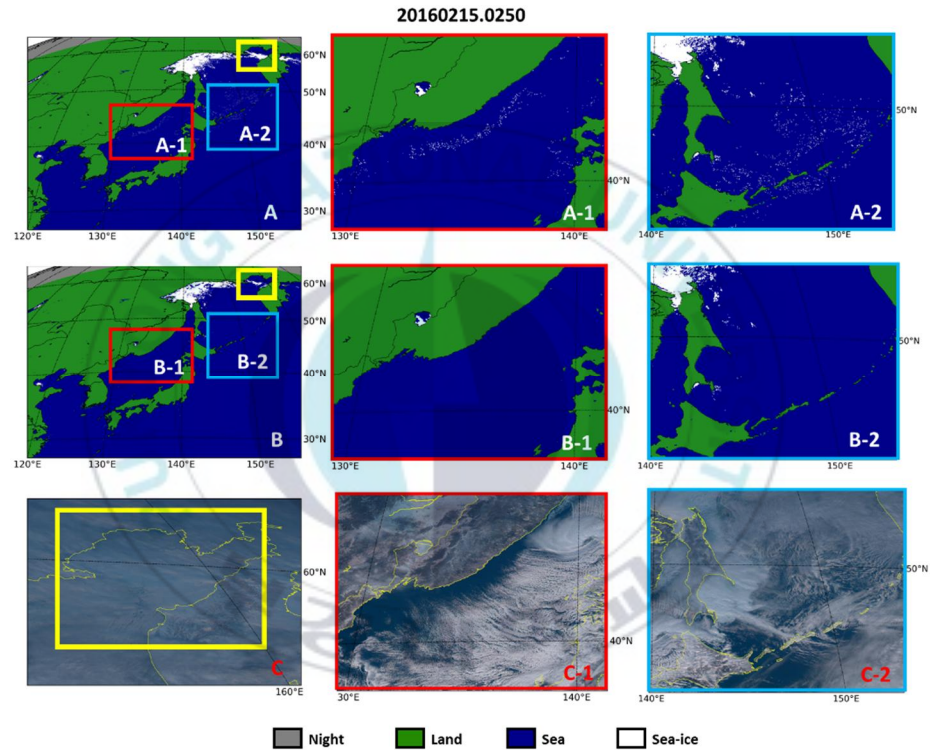


**Figure 22.** Addition test to sea-ice pixel detected DWW and  $IST_0$  test before (A) and after (B), (A-1, B-1, C-1) shows before, after and AHI RGB image on red box, (A-2, B-2, C-2) shows before, after and AHI RGB image on blue box, (C) shows before, after and AHI RGB image on yellow box.

### 3.8. Cloud re-check

Sea-ice detection using satellite data is important to discriminate sea-ice and cloud. Although this algorithm uses clear sky condition, cloud pixel still exist on the area. The red box on Figure 23 is sea-ice area according to AHI RGB image, but AHI image applied cloud showed it to cloud area. This part of this algorithm was performed to compensate for this phenomenon.

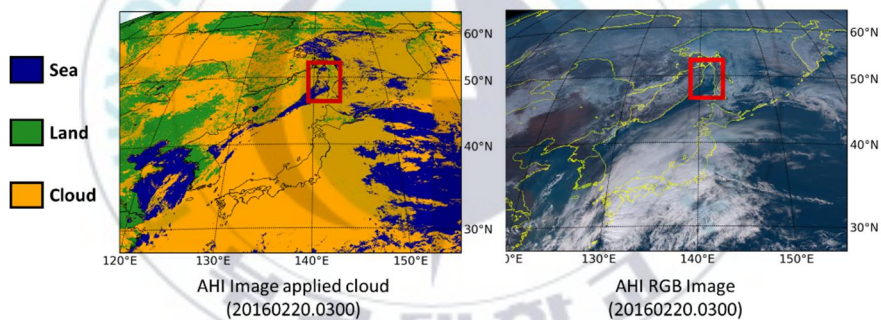


Figure 23. Comparison between AHI image applied cloud (left) and AHI RGB image (right).

#### 3.8.1. Difference [Snow spectral library $R_{1.61\mu\text{m}}$ -Profile $R_{1.61\mu\text{m}}$ ] test

The  $1.61 \mu\text{m}$  reflectance is important to discriminate cloud and sea-ice/snow. Typical snow/sea-ice has low reflectance at  $1.6 \mu\text{m}$ , while clouds have relatively high reflectance compared to snow/sea-ice due to small

grain size and low moisture content. In this fact, it is used to detect snow/sea-ice (Hall *et al.*, 2001) and it used to calculate NDSI. We used difference between  $R_{1.61 \mu\text{m}}$  snow spectral library and  $R_{1.61 \mu\text{m}}$  sea-ice candidate. The Figure 24 is shown in histogram which is difference between  $R_{1.61 \mu\text{m}}$  snow library and  $R_{1.61 \mu\text{m}}$  sea-ice candidate (profile). If the difference is over 0.12, the pixel is discriminated to sea-ice.

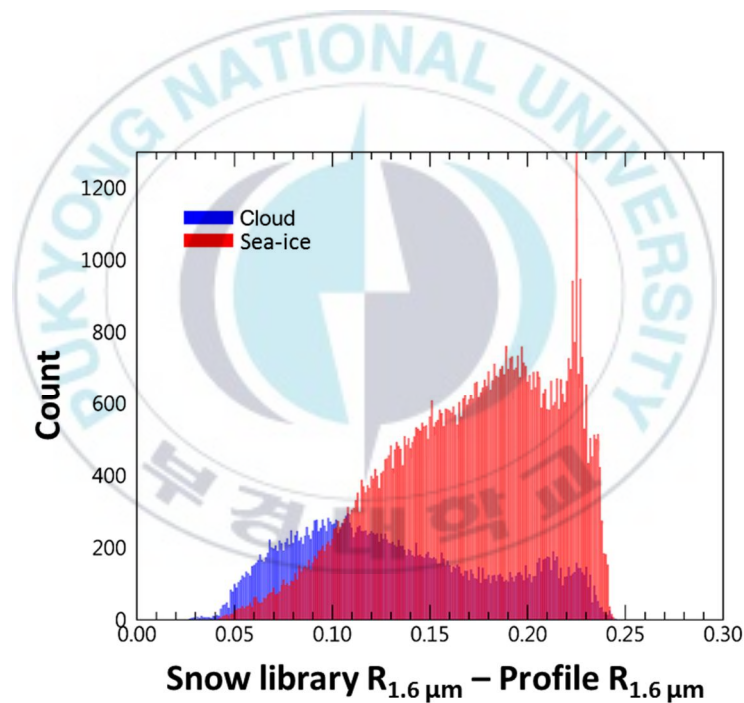


Figure 24. The difference [Snow spectral library  $R_{1.6 \mu\text{m}}$  - Profile  $R_{1.6 \mu\text{m}}$ ] histogram of sea-ice.

### 3.8.2. NDSI & BTD[11.0-3.8 $\mu\text{m}$ ] test

The NDSI & BTD test is performed only for pixels classified as sea-ice through difference [snow spectral library  $R_{1.61 \mu\text{m}} - R_{1.61 \mu\text{m}}$ ] test. NDSI is an index for estimating snow/sea-ice, but it is difficult to distinguish between snow/sea-ice and cloud when there is a mixture of upper cloud and snow/sea-ice. To solve this problem, the difference between the  $BT_{11 \mu\text{m}}$  and  $BT_{3.7 \mu\text{m}}$  (BTD) was used. BTD is mainly used for the detection of upper cloud mixed with snow/sea-ice, low value in snow/sea-ice and relatively high value in upper cloud. Therefore, in this study, if a pixel classified as snow/sea-ice through a was satisfying NDSI  $\cdot$  BTD test, it was not detected as sea-ice. Figure 25 (a) are before NDSI and BTD test and Figure 25 (b) are after NDSI and BTD test. Figure 25 (c) are AHI RGB image on that time. Before applying NDSI and BTD test, some clouds were detected as sea-ice, but after application, the amount of false positives decreased considerably.

The Figure 26 showed in sea-ice data using this algorithm.



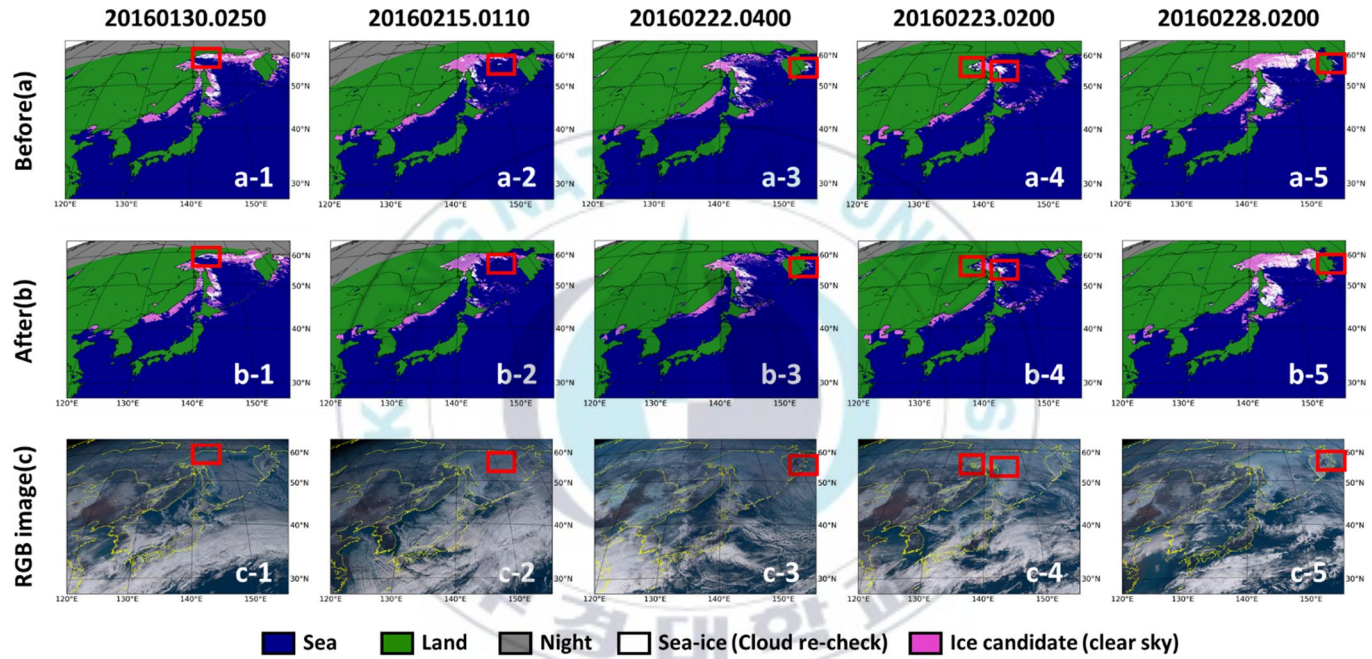
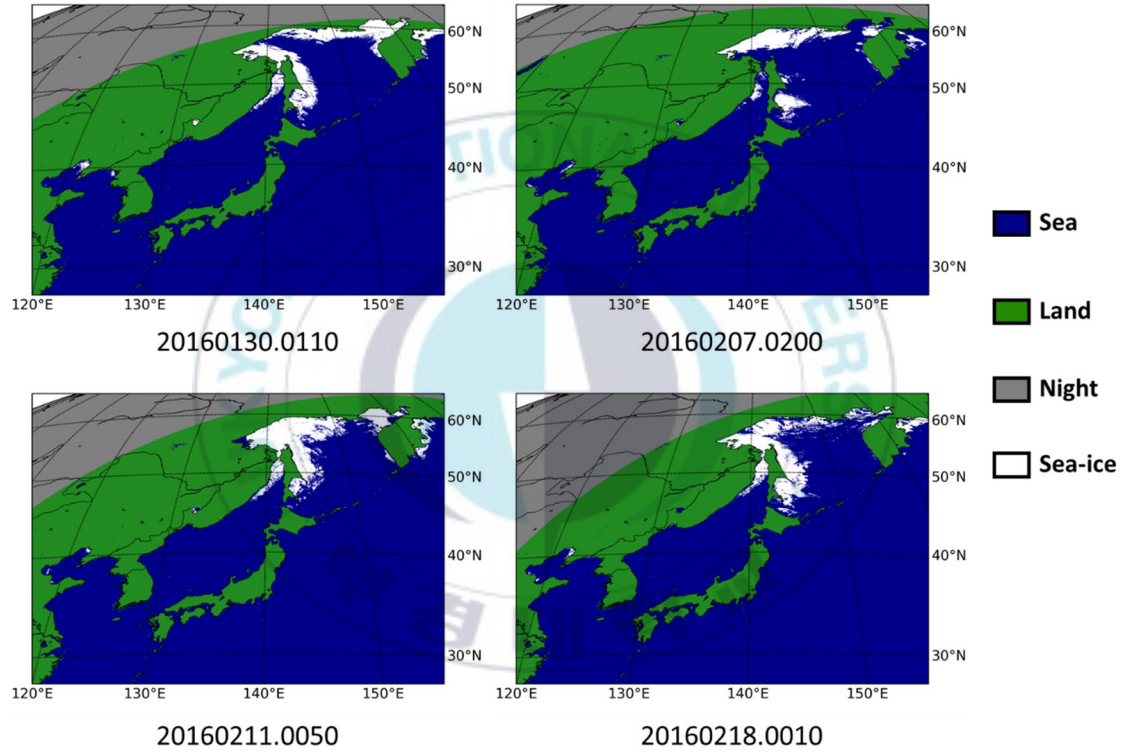


Figure 25. Comparison NDSI-BTD test before(a), after(b) and RGB image(c).



**Figure 26.** The sea-ice data using AH1 channel data on this study.

## 4. Validation evaluation

### 4.1. Validation strategy

The validation of sea-ice detection judges whether sea-ice exists or not. It is better than quantitative or qualitative expression. In this reason, we used categorical validation method. It uses forecast and observation pairs based on threshold criteria that define the categories. Based on the defined categories, a variety of statistical measures are computed. Categorical validation methodologies can be applied to either deterministic or probabilistic forecasts. Some scores are used specifically with deterministic forecast validation, and others are used with probabilistic forecasts. Table 4 is showed in contingency table. Contingency table is used to describe the distribution of forecasts and observations in terms of their frequencies for the difference categories. For validation with two categories, the 2x2 contingency table is commonly defined. It is for a yes/no configuration; in this study, sea-ice/no sea-ice. For this yes/no table, the rows represent this algorithm output (estimation) and the columns represent categories for validation data (observations). In a sea-ice/no sea-ice categorization, “Yes” represents “Sea-ice”, either validation and/or estimation. “No” represents “No sea-ice” either validation and/or

estimation. The “a” bin indicates the number of detected sea-ice that were correctly validation to be sea-ice, or hits. The “b” bin indicates the number of detected no sea-ice that had been incorrectly validation to be sea-ice, or false alarms. The “c” bin indicates the number of detected sea-ice that were validation to be no sea-ice, or misses. The “d” bin indicates the detected no sea-ice that were correctly validation to be no sea-ice, or correct negatives. “a+c” and “b+d” are the total detected sea-ice and no sea-ice respectively. “a+b” and “c+d” are the total validation sea-ice and no sea-ice respectively.

**Table 4. Contingency table on this study**

Estimation	Validation		Total
	Yes	No	
Yes	a (hit)	b (false)	a+b
No	c (miss)	d (correct rejection)	c+d
Total	a+c	b+d	a+b+c+d

The Probability of Detection (POD) is proportion of validation data that were detected to be sea-ice. The POD, or hit rate, in the case of sea-ice/no sea-ice, is the proportion of sea-ice of the VIIRS sea-ice data that

were detected to be sea-ice on this algorithm. It can range from a worse case of 0 to a perfect score of 1, or 100 %. The Equation 12 for calculating POD is as follows.

$$\mathbf{POD} = \frac{\mathbf{a}}{\mathbf{a} + \mathbf{c}} \quad \text{Equation 12}$$

The False Alarm Ratio (FAR) is proportion of validation data that were not detected to be sea-ice. The FAR in our case is the proportion of detected sea-ice on this algorithm that were not detected to be sea-ice on VIIRS sea-ice data. A perfect score is 0 and the worst possible score is 1. The Equation 13 for calculating FAR is as follows.

$$\mathbf{FAR} = \frac{\mathbf{b}}{\mathbf{a} + \mathbf{b}} \quad \text{Equation 13}$$

The Comparison Index (CI) is the square root of the value of POD and (1-FAR) to compare two data to show overall accuracy. The Equation 14 for calculating CI is as follows.

$$\mathbf{CI} = \sqrt{\mathbf{POD} \times (\mathbf{1} - \mathbf{FAR})} \quad \text{Equation 14}$$

The Correct Detection Ratio (CDR) is defined as the ratio of true pixels to total pixel. The true pixels are defined as the sum of Hit and Correct-Rejection when compared with VIIRS. The Equation 15 for calculating CDR is as follows.

$$\mathbf{CDR} = \frac{\mathbf{a + d}}{\mathbf{a + b + c + d}} \quad \text{Equation 15}$$

## 4.2. Qualitative evaluation

On this study, we used VIIRS sea-ice data to evaluate our sea-ice output. But, the observation area of VIIRS sea-ice data is based on SWATH onboard polar-orbiting satellites and AHI data which used as channel data in this algorithm, is based on geostationary satellites. Therefore, we converted the VIIRS sea-ice data into geostationary data suitable for the Himawari-8 observation area. Figure 27 shows VIIRS SWATH sea-ice data and after match-up work, on the AHI map.

20160229.0328

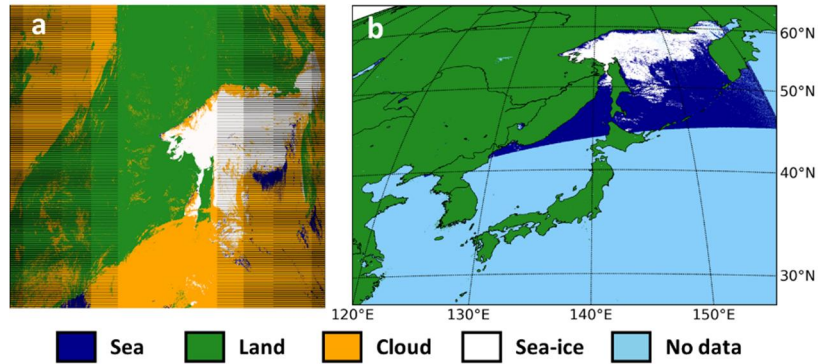


**Figure 27. (a) shows VIIRS SWATH sea-ice data, (b) shows VIIRS sea-ice data performed match-up on the Himawari8 observation area.**

In addition, since the AHI channel data used in this study have been produced data every 10-minute, the sea-ice data calculated by our algorithm is also produced at intervals of 10-minute. On the other hand, the temporal range of the VIIRS sea-ice data is from 5- to 6-minute. For this reason, we matched between AHI and VIIRS data as difference between AHI and VIIRS time interval is lower 4-minute. And the VIIRS data on the AHI map worked this process had a gap on the AHI FD. Therefore, the algorithm resolves to exclude pixel gaps in the validation of this algorithm sea-ice data. In this study, we used the categorical validation method used for mutual validation between satellite to verify the pixel detected by sea-ice. Using it, POD, FAR, CI and CDR were calculated and the accuracy of this study was quantified. The algorithm was tested using

VIIRS sea-ice characterization data from study area for the period of December 2015 to February 2016.

We performed to verify with 30 scenes on VIIRS sea-ice data during temporal range on this study. As result on this algorithm, The POD is 90.62 %, FAR is 1.72 %, CI is 94.37 % and CDR is 95.88 %. The GOES-R/ABI, which is a geostationary satellite, has a 87.6 % CDR accuracy and The AMSR-E of Aqua has  $97.2 \pm 3.6$  % CDR accuracy. Compared with other satellite sea-ice data, the accuracy of the sea-ice data of this algorithm is similar or higher. The Table 5 is detailed validation score compared with VIIRS sea-ice data. However, since VIIRS sea-ice data is based on single/multi-channel and IST based threshold method, it is still possible to detect potential miss and false possibility such as previous sea-ice detection studies. Therefore, To more accurately evaluate the results of this study, additional qualitative validation was performed using AHI RGB image.



**Table 5. Validation score compared with VIIRS sea-ice data; hit is sea-ice (both sea-ice algorithm and VIIRS sea-ice data, false is sea-ice on this algorithm and no sea-ice on VIIRS sea-ice data, miss is no sea-ice on this algorithm and sea-ice on VIIRS sea-ice data, correct-reject is no sea-ice (both this algorithm and VIIRS sea-ice data)**

Hit	False	Miss	Cor-reject	POD	FAR	CI	CDR
<b>533,440</b>	9,623	66,385	1,054,533	90.62	1.72	94.37	95.88
<b>(pixel)</b>	(pixel)	(pixel)	(pixel)	(%)	(%)	(%)	(%)

### 4.3. Quantitative evaluation

In the quantitative evaluation, we used AHI RGB image for evaluating sea-ice data on this algorithm additionally. Another fact for using AHI RGB image Another reason for using AHI RGB image is to further evaluate areas except for the area provided by VIIRS sea-ice data. Since VIIRS sea-ice data is onboarded on polar-orbit satellites, it has been provided information on limited area every 5-minute. Because of this, we can compare the sea-ice data detected by this algorithm only in the area provided by VIIRS sea-ice data.

The Figure 28, Figure 29, Figure 30 are showed in comparison between sea-ice algorithm and VIIRS sea-ice data and AHI RGB image. The purple box (a), (b) on the Figure 28 is showed to miss detection of sea-ice pixel. As we analyzed to the area in more detail, the pixels in the area were

detected as noise. Compared with AHI RGB image, the area is a region where cloud and ice-free water are mixed, and there isn't sea-ice. In this reason, it is judged that the area isn't detected by this algorithm but detected by VIIRS sea-ice data. The purple box (a) on Figure 29 is also showed to miss detection of sea-ice pixel. The non-detected area at that date also performed a detailed analysis. As result of the analysis, it was found that the area of the detection pixels was like noise and the area where clouds and ice-free water were mixed when compared with AHI RGB images. The purple box (a) on Figure 30 is also showed in previous analysis result. The red box (b) on Figure 30 is also showed miss detection pixels on the specific area. As result of comparison analysis with the AHI RGB image, the region was the sea-ice region mixed with the ice-free water. These miss-detected pixels showed to specific feature. It is located on boundary between land and sea.

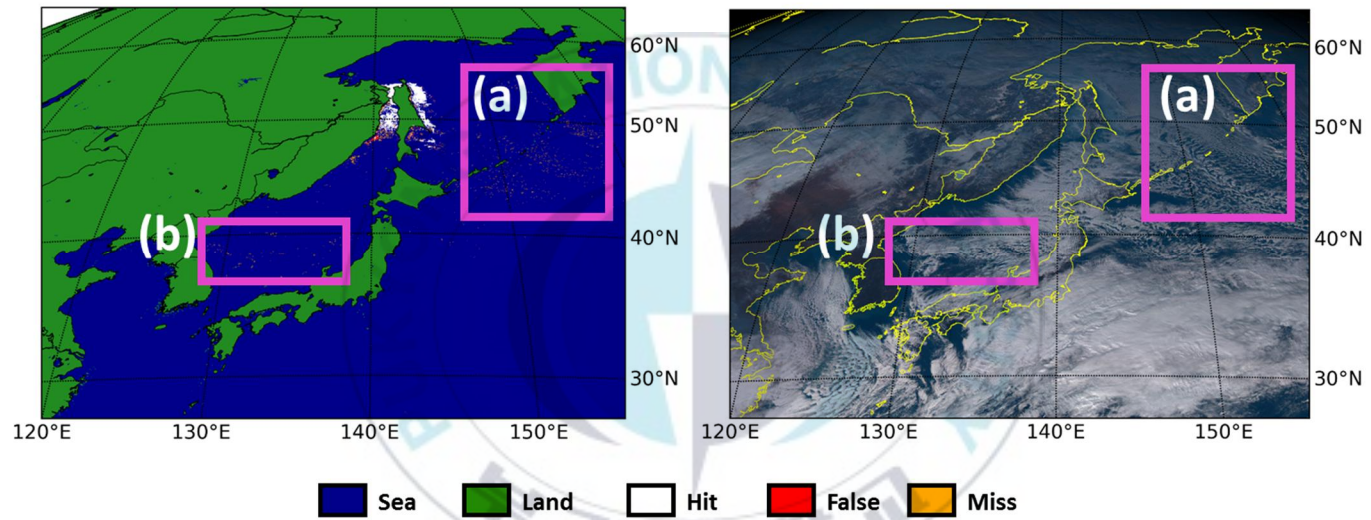


Figure 28. Comparison image between sea-ice algorithm and VIIRS sea-ice data (left side), AHI RGB image (right side), 20160112.0330 (UTC).

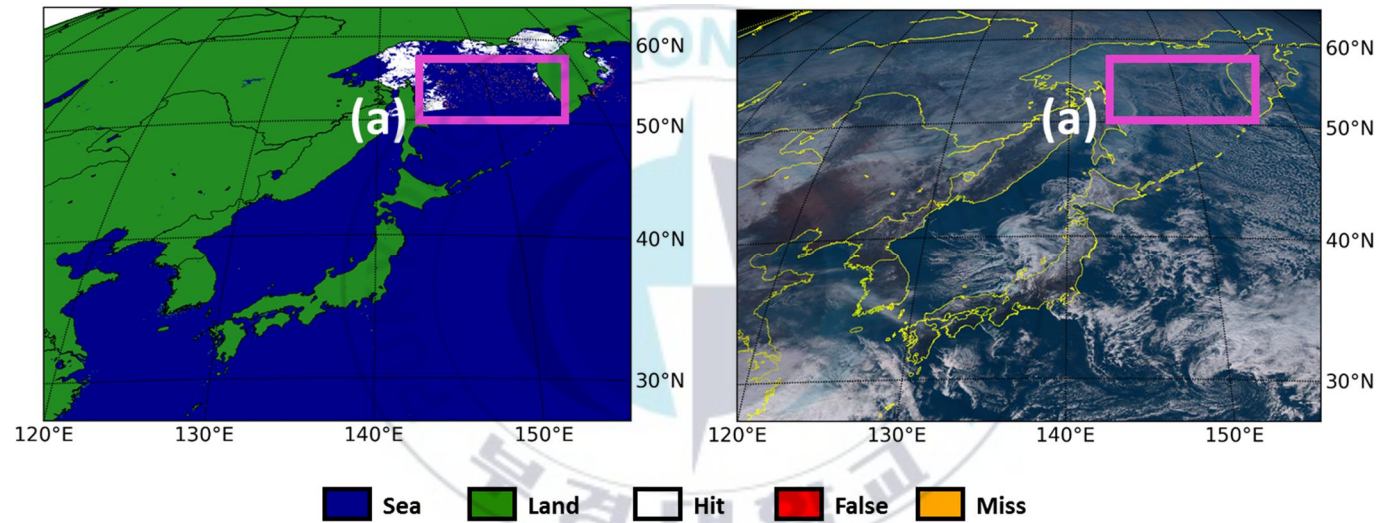
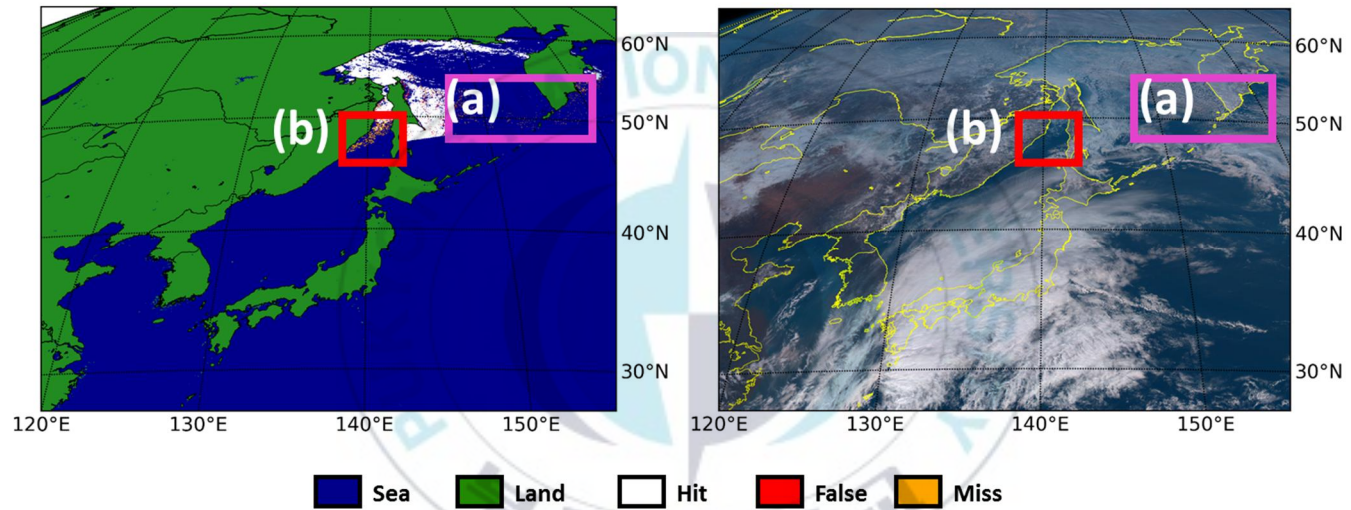


Figure 29. Comparison image between sea-ice algorithm and VIIRS sea-ice data (left side), AHI RGB image (right side), 20160204.0300 (UTC).



**Figure 30. Comparison image between sea-ice algorithm and VIIRS sea-ice data (left side), AHI RGB image (right side), 20160220.0300 (UTC).**

## 5. Summary and Conclusion

The previous studies and advanced organization for sea-ice detection is mostly used static threshold method using satellite channel data. The static threshold method can't consider to variability of reflectance on sea-ice. For this reason, this study proposed a new hybrid-dynamic thresholding technique that combines static threshold method, DWW method, and  $IST_0$  method considering sea-ice reflectance variability.

We detected sea-ice using AHI data onboard Himawari-8 geostationary satellite which can be observed 24-hour in constant observation area. The AHI instrument onboard Himwari-8 has produced channel data in 10-minutes. This study has detected sea-ice using AHI channel data with these characteristics. By using AHI channel data with this characteristic, this study has an advantage in detecting sea-ice with temporal and spatial continuity.

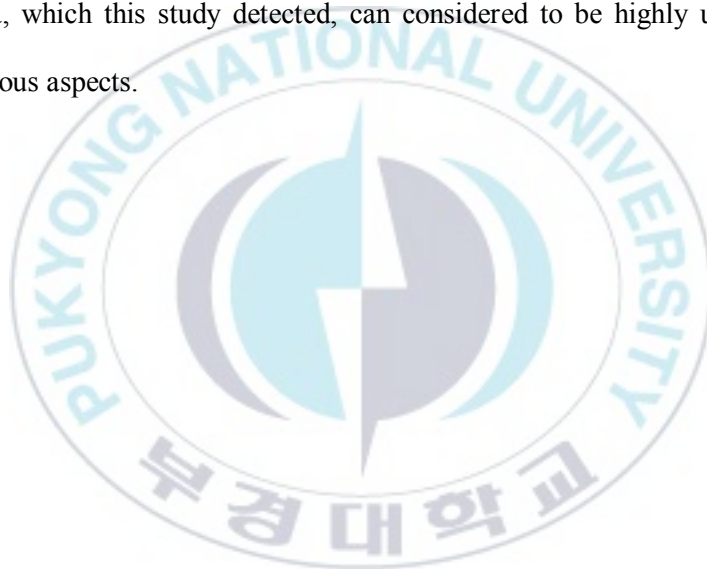
We analyzed sea-ice data detected by this algorithm. First, we built ancillary data using satellite data prior to performing this algorithm. The ancillary data are long-term satellite based sea-ice data using NSIDC weekly snow and sea-ice extent data and snow spectral library using MODIS snow cover product (MOD10\_L2) and performed pre-processing;

Normalization of the AHI channel data using SZA and discrimination to sea-ice candidate pixel. Next, we performed to detect sea-ice using threshold, DWW,  $IST_0$  test. First, we used the static threshold method to distinguish confident sea-ice and ice-free water. The pixels of the sea-ice candidate, which can not be distinguished by the static threshold method, secondarily detected sea-ice using the DWW method to account for the snow covered ice. For the pixels not distinguished by the DWW method,  $IST_0$  method was used to distinguish the sea ice from the third one. In addition, Ice re-check was performed on the sea ice pixels separated by DWW and  $IST_0$  method, and cloud re-check was performed on the previously separated clouds.

The accuracy of this algorithm is similar or higher than others sea-ice detection algorithm. In addition to quantitative evaluation, qualitative evaluation was also performed using AHI RGB image. Through qualitative evaluation, the sea-ice detection algorithm had high similarity and showed the following characteristics. One feature is that the false detection rate of the sea-ice is low in the cloud region which is difficult to distinguish from the sea ice. Especially, the VIIRS sea-ice data, which is the validation data, have many areas where false sea-ice is detected in the region where cloud and ice-free water are mixed. On the other hand, the area was separated to the ice-free water on this study. In this way, the proposed sea-ice detection

algorithm showed high accuracy through quantitative and qualitative evaluation and this study detected sea-ice using geostationary satellite data, not polar orbiting satellite such as MODIS, VIIRS.

In addition, the sea ice data produced by the new hybrid-dynamic thresholding technique is used in various industrial areas such as weather and climatic aspects and shipping transportation. Therefore, the sea-ice data, which this study detected, can be considered to be highly utilized in various aspects.





## 6. References

- Allison, I., J. Carrasco, G. Kaser, R. Kwok, P. Mote, T. Murray, F. Paul, J. Ren, E. Rignot, O. Solomina, K. Steffen, T. Zhang, 2014, *IPCC Fifth assessment report, WGI chapter 4: Observations: Cryosphere (2014)*, European Climate Adaptation Platform.
- Baker C. B., and A. H. Strahler, 1993, Solar Zenith Angle Effects on Forest Canopy Hemispherical Reflectances Calculated with a Geometric-Optical Bidirectional Reflectance Model, *IEEE Transactions on Geoscience and Remote Sensing*, Vol. 31, NO. 4, July, 1993.
- Bell R. E., Chu W., Kingslake J., Das I., Tedesco M., Tinto K. J., Zappa C. J., Rrezzotti M., Boghosian A. And Lee W. S., 2017, Antarctic ice shelf potentially stabilized by export of meltwater in surface river, *Nature*, Vol. 544.
- Belward, A. S., Estes, J. E., & Kline, K. D. (1999). The IGBP-DIS Global 1-km Land-Cover Data Set DISCover: A Project Overview. *Photogrammetric Engineering and Remote Sensing*, 65, 1013-1020.
- Friedl, M. A., McIver, D. K., Hodges, J. C. F., Zhang, X. Y., Muchoney, D., Strahler, A. H., Woodcock, C. E., Gopal, S., Schneider, A., Cooper, A., Baccini, A., Gao, F., & Schaaf, C. (2002). Global land

- cover mapping from MODIS: algorithm and early results. *Remote Sensing of Environment*, 83, 287-302.
- Friedl, M. A., Sulla-Menashe, D., Tan, B., Schneider, A., Ramankutty N., Sibley, A., & Huang, X. (2010). MODIS Collection 5 global land cover: Algorithm refinements and characterization of new datasets. *Remote Sensing of Environment*, 114, 168-182.
- Hall, D. K. and Riggs G. A., 2007, Accuracy assessment of the MODIS snow products, *Hydrological Processes*, 21, 1534-1547.
- Hall, D. K., Riggs G. A., Salomonson V. V., Barton J. S., Casey K., Chien J. Y. L., DiGirolamo N. E., Klein A. G., Powell H. W., and Tai A. B., 2001, Algorithm Theoretical Basis Document (ATBD) for the MODIS snow and sea-ice mapping algorithms, NASA GSFC, September.
- Hall, D. K., Key J. R., Casey K. A., Riggs G. A., Cavalieri D. J., 2004, Sea ice surface temperature product from MODIS, *IEEE Transactions on Geoscience and Remote Sensing*, Vol 42, No. 5, May 2004.
- Huggel, C. 1998, *Periglaziale Seen im Luft- und Satellitenbild*. Diploma thesis, Department of Geography, University of Zurich.
- Huggel, C., Käab, A., Haeberli, W., Teysseire, P., and Paul, F. 2002, Remote sensing based assessment of hazards from glacier lake outbursts: a case study in the Swiss Alps. *Can. Geotech. J.*, 39, 316-

330.

- Jin, D. H., K. S. Lee, S. W. Choi, M. J. Seo, D. L. Lee, C. Y. Kwon, H. H. Kim, Y. K. Lee and K. S. Han, 2017, Determination of dynamic threshold for sea-ice detection through relationship between 11  $\mu\text{m}$  brightness temperature and 11-12  $\mu\text{m}$  brightness temperature difference, *Korean Journal of Remote Sensing*, Vol. 33, No.2, 2017, pp.243-248.
- Johannessen O. M., L. Bengtsson, M. W. Miles, S. I. Kuzmina, V. A. Semenov, G. V. Alekseev, A. P. Nagurnyi, V. F. Zakharov, L. P. Bobylev, L. H. Pettersson, K. Hasselmann and H. P. Cattle, 2004, Arctic climate change: observed and modelled temperature and sea-ice variability, *Tellus*, 56A, 328-341.
- Kawano K. and J. I. Kudoh, 2004, Monitoring of Sea Ice in Far East Russia, Geoscience and Remote Sensing Symposium, 2004, IGARSS '04. Proceedings. 2004 IEEE International.
- Keogh, E., M. Pazzani, 2001. Derivative dynamic time warping. In: First SIAM International Conference on Data Mining (SMD'2001), Chicago, Illinois.
- Key J. and M. Haefliger, 1992, Arctic Ice Surface Temperature Retrieval from AVHRR Thermal Channels, *Journal of Geophysical Research*, Vol, 97, No. D5, Pages 5885-5893.

- Key, J. R., J. B. Collins, C. Fowler and R. S. Stone, 1997, High-Latitude Surface Temperature Estimates from Thermal Satellite Data, *Remote Sensing Environment*, 61:302-309.
- Key, J. R., R. Mahoney, Y. Liu, P. Romanov, M. Tschudi, I. Appel, J. Maslanik, D. Baldwin, X. Wang, and P. Meade, 2013, Snow and ice products from Suomi NPP VIIRS, *Journal of Geophysical Research: Atmosphere*, 118(23):12816-12830.
- Lee K. S., D. H. Jin, J. M. Yeom, M. J. Seo, S. W. Choi, J. J. Kim, and K. S. Han, 2017, New Approach for Snow Cover Detection through Spectral Pattern Recognition with MODIS Data, *Journal of Sensors*, Volume 2017, Article ID 4820905, 15 Pages.
- Liu Y., J. R. Key, 2010, ABI Ice Cover and Concentration Algorithm Theoretical Basis Document (ATBD), NOAA NESDIS center for satellite applications and research.
- Parkinson, C. L., J. C. Comiso, H. J. Zwally, D. J. Cavalieri, P. Gloersen and W. J. Campbell, 1987, Arctic sea ice, 1973-1976: *Satellite passive-microwave observations*, NASA SP-489, GPO, Washington, D. C., USA.
- Paul, F., 2007, The New Swiss Glacier Inventory 2000 – Application of Remote Sensing and GIS. Schriftenreihe Physische Geographie, Universität Zurich, 52, 210 pp.

- Petitjean, F., J. Inglada, and P. Gançarski, 2012. Satellite image time series analysis under time warping, *Geoscience and Remote Sensing, IEEE Transactions on*, 50(8): 3081-3095.
- Riggs, G. A., D. K. Hall, S. A. Ackerman, 1999, Sea Ice Extent and Classification Mapping with the Moderate Resolution Imaging Spectroradiometer Airborne Simulator, *Remote Sensing of Environment* Volume 68, Issue 2, May 1999, Pages 152-163.
- Schaaf C. B. and Strahler A. H., 1993. Solar Zenith Angle Effects on Forest Canopy Hemispherical Reflectances Calculated with a Geometric-Optical Bidirectional Reflectance Model, *IEEE Transactions on geoscience and Remote Sensing*, Vol. 31, No. 4.
- Scepan, J. 1999. Thematic Validation of High-Resolution Global Land-Cover Data Sets, *Photogrammetric Engineering and Remote Sensing*, 65, 1051-1060.
- Seo, M., H. C. Kim, M. huh, J. M. Yeom, C. S. Lee, K. S. Lee, S. W. Choi and K. S. Han, 2016, Long-term variability of surface albedo and its correlation with climatic variables over Antarctica, *Remote Sensing*, 8(12): 981.
- Tucker C. J., 1979, Red and Photographic Infrared Linear Combinations for Monitoring Vegetation, *Remote Sensing of Environment* 8:127-150.

Zhang Z., P. Tang and R. Duan, 2015, Dynamic time warping under pointwise shape context, Information Sciences 315 (2015) 88-101.

